A&A 529, A72 (2011)
DOI: 10.1051/0004-6361/200913498

Astronomy & Astrophysics

On the evolution of environmental and mass properties of strong lens galaxies in COSMOS⋆

C. Faure[1], T. Anguita[2,3], D. Alloin[4], K. Bundy[5], A. Finoguenov[6], A. Leauthaud[7,8], C. Knobel[9], J.-P. Kneib[10], E. Jullo[11], O. Ilbert[10], A. M. Koekemoer[12], P. Capak[13], N. Scoville[13], and L. A. M. Tasca[10]

[1] Laboratoire d'Astrophysique, École Polytechnique Fédérale de Lausanne (EPFL), Observatoire de Sauverny, 1290 Versoix, Switzerland
[2] Centro de Astro-Ingeniería, Departamento de Astronomía y Astrofísica, Pontificia Universidad Católica de Chile, Casilla 306, Santiago, Chile
[3] Max Planck Institut für Astronomia, Königstuhl 17, 69117 Heidelberg, Germany
[4] Laboratoire AIM, CEA/DSM-CNRS-Universite Paris Diderot, IRFU/SEDI-SAP, Service d'Astrophysique, CEA Saclay, Orme des Merisiers, 91191 Gif-sur-Yvette, France
[5] Hubble Fellow, Department of Astronomy, UC Berkeley, 601 Campbell Hall, Berkeley, CA 94720-3411, USA
[6] Max-Planck Institut für Extraterrestrische Physik, Giessenbachstrasse, 85748 Garching, Germany
[7] Lawrence Berkeley National Laboratory, 1 Cyclotron Road, Berkeley CA 94720, USA
[8] Berkeley Center for Cosmological Physics, University of California, Berkeley, CA 94720, USA
[9] Institute for Astronomy, ETH Zurich, Wolfgang-Pauli-Strasse 27, 8093 Zurich, Switzerland
[10] Laboratoire d'Astrophysique de Marseille, CNRS Université de Provence, 38 rue F. Joliot-Curie, 13388 Marseille Cedex 13, France
[11] Jet Propulsion Laboratory, MS 169-327,4800 Oak Grove Drive, Pasadena, CA 91109, USA
[12] Space Telescope Science Institute, 3700 San Martin Drive, Baltimore, MD 21218, USA
[13] California Institute of Technology, MC 105-24, 1200 East California Boulevard, Pasadena, CA 91125, USA

Received 19 October 2009 / Accepted 12 February 2011

ABSTRACT

Context. Nearly 100 new strong-lens candidates have been discovered in the COSMOS field. Among these, 20 lens candidates with $0.34 \lesssim z_{\rm lens} \lesssim 1.13$ feature multiple images of background sources.
Aims. Using the multi-wavelength coverage of the field and its spectroscopic follow-up, we characterize the evolution with redshift of the environment and of the dark-matter (DM) fraction of the lens galaxies.
Methods. We present spectroscopic and new photometric redshifts of the strong-lens candidates. The lens environment is characterized in the following way: we account for the projected 10 closest galaxies around each lens and for galaxies with a projected distance less than 1 Mpc at the lens galaxy redshift. In both cases, we perform similar measurements on a control sample of "twin" non-lens early-type galaxies (ETGs). In addition, we identify group members and field galaxies in the X-ray and optical catalogs of galaxy groups and clusters. From those catalogs, we measure the external shear contribution of the groups/clusters surrounding the lens galaxies. The systems are then modeled using a singular isothermal ellipsoid for the lens galaxies plus the external shear produced by the groups/clusters.
Results. We observe that the average stellar mass of lens galaxies increases with redshift. In addition, we measure that the environment of lens galaxies is compatible with that of the twins over the whole redshift range tested here. During the lens modeling, we notice that when let free, the external shear points in a direction which is the mean direction of the external shear produced by the groups/clusters and of the closest galaxy to the lens. We also notice that the DM fraction of the lens galaxies measured within the Einstein radius significantly decreases as the redshift increases.
Conclusions. Given these observations, we conclude that while the environment of lens galaxies is compatible with that of non-lens ETGS over a wide range of redshifts, their mass properties evolves significantly with redshift: it is still not clear whether this advocates in favor of a stronger lensing bias toward massive objects at high redshift or if it is simply representative of the high proportion of massive and high stellar density galaxies at high redshift.

Key words. gravitational lensing: strong

1. Introduction

In the field of gravitational lensing, studies of strong galaxy-galaxy lenses on statistical grounds have recently become possible. Indeed, within just a few years, searches in the SDSS (SLACS: Bolton et al. 2006, 2008; Allam et al. 2007), in COSMOS (Faure et al. 2008, hereafter Paper I; Jackson 2008), and in the CFHT-LS surveys (SL2S: Cabanac et al. 2007; Limousin et al. 2009b) have delivered more than two hundred new strong galaxy-galaxy lenses, which span a wide range in redshift and image angular separation. The reasons for this interest are manifold. First, strong-lens galaxies provide measurements of the total mass distribution on galaxy scales, which brings additional information about the processes of galaxy formation and evolution (e.g. Ofek et al. 2003; Chae et al. 2006; Koopmans et al. 2006; Tortora et al. 2010). Second, from a statistical point of view, strong lensing occurrences trace the

⋆ Based on observations made with ESO telescopes at Paranal observatory under program ID 077.A-0473(A) and under large program ID 175.A-083911.

abundance and concentration of matter in the universe, which provides another test for cosmological models (e.g. Keeton 2001; Bartelmann et al. 2003).

Studies of the physical and environmental properties of low-redshift strong-lens galaxies ($z \lesssim 0.3$) have shown that they are bona fide massive early-type galaxies (ETGs; Treu et al. 2006, 2009, T09 hereafter; Gavazzi et al. 2007; Grillo et al. 2009). The strong-lens sample in the COSMOS field (Paper I) spans a higher redshift range ($0.33 \leq z \leq 1.13$) and previous work on this sample have shown that the projected distribution of lens galaxies in COSMOS is comparable to that of ETGs, whether in rich environments such as cosmic filaments, or in the field (Faure et al. 2009, hereafter Paper II). Interestingly, this result means that multiple-mass-sheets do not contribute significantly to make more efficient lenses, contrary to results found in ray tracing through numerical simulations (Wambsganss et al. 2005; Hilbert et al. 2007, 2008). In Paper II we also demonstrate that the presence of large scale structures (LSS) in the lens galaxy environment increases the angular separation of the lensed images of a source, as noticed earlier by Oguri et al. (2005).

In addition, analyses of the mass density profiles of strong-lens galaxies from hydrodynamical N-body simulations (Dobke et al. 2007; Limousin et al. 2009a) and lens samples (Limousin et al. 2007; Auger 2008; Natarajan et al. 2009) show that the mass distribution in galaxies depends on their environment. For example, compared to galaxies centrally placed in their group or cluster, some skewing of the total mass density slope appears in galaxies located at the edges of a group or cluster. This is consistent with tidal stripping of their dark matter halo (T09).

Therefore, it is important to explore the local environment of the COSMOS strong-lenses rather than in LSS as in Paper II. We also aim to learn about the lens galaxy mass properties, in particular to derive information relative to their dark matter (DM) fraction ($f_{\rm DM}$, defined as $f_{\rm DM} = 1 - M_\star/(M_\star + M_{\rm DM})$. This is possible because the COSMOS strong-lenses pertain to one of the best-studied regions of the sky, for which deep multi-wavelength observations have been collected (Koekemoer et al. 2007; Taniguchi et al. 2007; Capak et al. 2007a; Scoville et al. 2007; Lilly et al. 2007; Ilbert et al. 2009). Thus, the properties of the COSMOS galaxy population have been studied extensively (e.g. McCracken et al. 2007; Capak et al. 2007b; Scarlata et al. 2007a,b; Ilbert et al. 2010).

The paper is organized as follows. In Sect. 2 we provide improved redshifts and stellar masses of the COSMOS lens galaxies. In Sect. 3 we examine and discuss the lens environment. In Sect. 4 we present results from our strong-lens mass models for the subsample of triple and quadruple image systems. Discussion and conclusions appear in Sect. 5. Throughout this paper, we assume a WMAP5 ΛCDM cosmology with $\Omega_{\rm m} = 0.258$, $\Omega_\Lambda = 0.742$, $H_0 = 72\ h_{72}$ km s^{-1} Mpc^{-1}.

2. The COSMOS sample of strong-lenses: new redshifts and stellar masses

By visual inspection of stamp images of $10'' \times 10''$ around ~9500 early photometric type galaxies (with redshifts: $0.2 \leq z \leq 1.0$, and absolute magnitude: $M_{\rm V} < -20$) in the COSMOS field, we have discovered 60 strong-lens candidates (Paper I). In addition, in the same study, 7 lens candidates were serendipitously found scattered across the field. Among the whole sample, 19 systems display long curved arcs or multiple images with similar colors (based on SUBARU images, by Taniguchi et al. 2007) around a bright-lens galaxy, and with an image arrangement around the lens galaxy which is consistent with the lensing hypothesis, as probed by lens modeling.

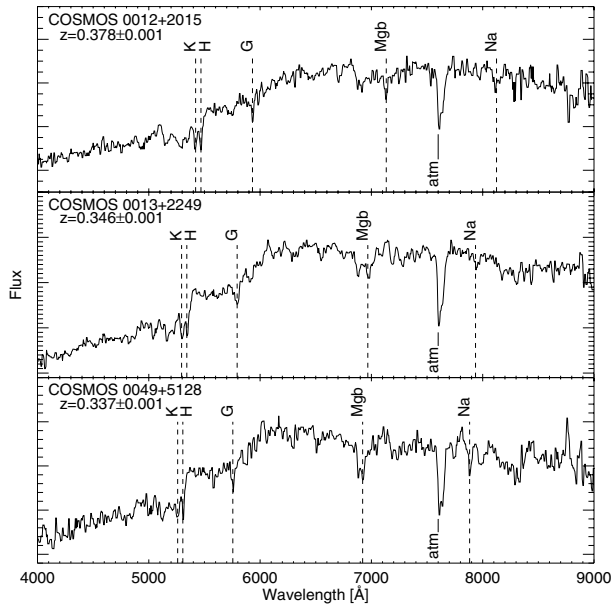

Fig. 1. VLT/FORS1 spectra of three strong-lens candidates. The spectral resolution is 5.52 Å per pixel, and has been smoothed by a 3-pixel box to improve the quality of the display. Flux is in arbitrary units.

Independently, Jackson (2008) inspected the complete set of galaxies in the COSMOS field, without discrimination. He has discovered two additional convincing strong-lens candidates that produce multiple images:J095930.93+023427.7 and J100140.12+020040.9. The lens galaxies both appear to be ETGs.

Among the 21 multiple-image lenses now available, one system (COSMOS 5921+0638) – which is the only confirmed lensed quasar of the sample – has been studied separately by Anguita et al. (2009, hereafter Paper III). Another system, COSMOS 5737+3424, is a galaxy cluster that is lensing a set of background galaxies. In such a case, the lens covers a different mass scale than in the other 20 systems, and the lens potential is more complex than a single lens galaxy: this target has been dropped from the present analysis.

2.1. Spectroscopic followup

On 2006 March 3 and 2006 April 25−26, we have successfully obtained spectra for five of the strong-lenses in the COSMOS field (PI: Faure) using the FORS1 instrument (ESO/VLT) in multi-object spectroscopic mode with 19 slits. For each target, the central slit was located on the lens candidate with an orientation intersecting both the lens galaxy and the brightest lensed image. The other 18 slits in the $\sim 7' \times 7'$ field around the lens, were preferentially positioned on galaxies with colors similar to that of the lens galaxy (likely at the same redshift). Leaving aside COSMOS 5921+0638 (discussed in Paper III) and the lens cluster COSMOS 5737+3424, we display the spectra of the other three lens galaxies in Fig. 1. Regarding the source redshifts, from this dataset we could extract only one source redshift, in COSMOS 5921+0638 (Paper III). Positions and redshifts of secondary targets around COSMOS 0012+2015, COSMOS 0013+2249 and COSMOS 0049+5128 are given in Table 2.

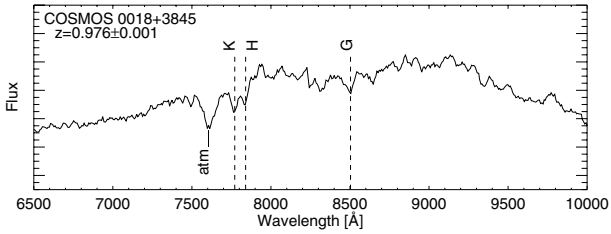

Fig. 2. Keck/DEIMOS spectrum of COSMOS 0018+3845. The spectrum is smoothed by 2.3 Å and binned down to 7.5 Å per pixel, taking the wavelength dependent noise into account to improve the apparent signal-to-noise. Flux is in arbitrary units.

In addition, several COSMOS lens candidates have been observed with the Keck telescopes. Using the Deep Extragalactic Imaging Multi-Object Spectrograph (DEIMOS), a spectrum of COSMOS 0018+3845 has been obtained on 2010 February 11 (Fig. 2). The data were collected in 7 × 1800 s exposures under photometric conditions with 0.5−0.7″ seeing. We used a 1″ slit together with the 830 line/mm grating tilted to 7860 Å and the OG550 blocking filter. The resulting spectral resolution is <3.3 Å, depending on seeing and object morphology. The objects were dithered along the slit by ±3″ between exposures to improve background subtraction, as described in Capak et al. (2011). The redshift of the lens was identified using the CaII H & K absorption lines and G-band. The source redshift is estimated based on the Lyman break, which is somewhere in the Subaru IA624-band ($\lambda_{\rm effective}$ = 6226 Å, $FWHM$ = 299 Å), and yields constraints on the source redshift: $3.9 < z_{\rm s} < 4.1$. From there, we find that for $z_{\rm s} = 3.96 \pm 0.02$, SiIV and CII would align with spectral absorption features of the lens. This estimation of the source redshift is used throughout the paper.

Moreover, with the Low Resolution Imaging Spectrometer (LRIS), Lagattuta et al. (2010) measured the redshifts for seven lens galaxies and two sources.

Finally, we retrieved the redshifts of seven strong-lens candidates from our list (based on the G-band and MgI absorption lines) from the z-COSMOS catalog (Lilly et al. 2009). Two of them, re-observed with Keck/LRIS, benefit from a second redshift determination from a higher signal-to-noise spectrum. Both redshifts agree.

A summary of the spectroscopic observations available for this sample is given in Table 1, while the lens redshifts are provided in Table 3.

2.2. Improved photometric redshifts

Recently a new set of photometric redshifts for galaxies in the COSMOS field has been derived by Ilbert et al. (2009), using the code *Le Phare* (Arnouts & Ilbert[1]) and the photometric dataset by Capak et al. (2007a, 2011). Compared to the previous set of COSMOS photometric redshifts by Mobasher et al. (2007), which relied on *8* broad bands, the main improvement is the use of *30* bands: the 8 broad bands plus 12 intermediate bands, 2 narrow bands, 7 bands in the near-infrared and 1 band in the ultra-violet. In Fig. 3 we display a comparison between the new photometric redshifts and spectroscopic redshifts for the 17 lens galaxies in our sample for which we have both measurements. For most lens galaxies, the agreement is good within the 68% confidence level error-bars measured for the photometric redshifts. Thus, these new photometric redshifts

[1] Available at www.oamp.fr/people/arnouts/LE_PHARE.html

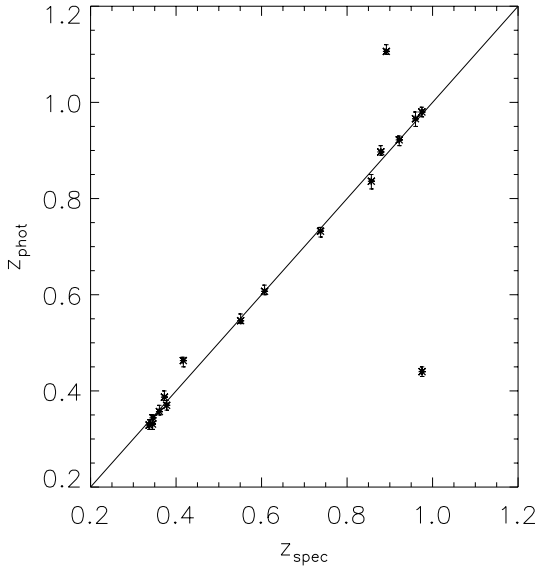

Fig. 3. Photometric redshift, $z_{\rm phot}$, versus spectroscopic redshift, $z_{\rm spec}$, for 16 of the lens galaxy candidates. The solid line features $z_{\rm phot} = z_{\rm spec}$. Errors bars on the value of $z_{\rm phot}$ relate to the 68% confidence level.

Table 1. Summary of the VLT (FORS1 and VIMOS) and Keck (DEIMOS and LRIS) observations: target name, instrument, and exposure time (in ks).

Name	Instr.	E.T. ks
COSMOS 0012+2015	FORS1	1.8
COSMOS 0013+2249	FORS1	1.2
COSMOS 0049+5128	FORS1	1.2
COSMOS 5921+0638	FORS1	1.8
COSMOS 0050+4901	VIMOS	3.6
COSMOS 0056+1226	VIMOS	3.6
COSMOS 5947+4752	VIMOS	3.6
J095930.93+023427.7	VIMOS	3.6
COSMOS 5857+5949	VIMOS	3.6
COSMOS 0124+5121	VIMOS	3.6
COSMOS 0227+0451	VIMOS	3.6
COSMOS 0018+3845	DEIMOS	12.6
COSMOS 0038+4123	LRIS	3.6
COSMOS 0050+4901	LRIS	5.4
COSMOS 0056+1226	LRIS	5.4
COSMOS 0211+1139	LRIS	5.4
COSMOS 0216+2955	LRIS	3.6
COSMOS 0254+1430	LRIS	1.2
J100140.12+020040.9	LRIS	5.4

Notes. Dispersion is 5.52 Å per pixel for FORS1/150I and 2.50 Å per pixel for VIMOS/MR/OS-red. The VIMOS redshifts were obtained from the z-COSMOS follow-up of the field (Lilly et al. 2007, 2009). The Keck/DEIMOS observations were taken with the 830 line/mm grating and using the OG550 blocking filter, which lead to a dispersion of 0.47 Å per pixel. The Keck/LRIS targets were simultaneously observed with both blue grating (300/5000, dispersion: 2.55 Å per pixel) and red grating (600/7500, dispersion: 1.28 Å per pixel) (see Lagattuta et al. 2010).

for the lenses are reliable estimates of their spectroscopic redshifts. Three systems show a strongly deviant photometric redshift (COSMOS 0254+1430: $z_{\rm phot} = 0.46 \pm 0.01$ and $z_{\rm spec} = 0.417 \pm 0.001$; J095930.93+023427.7: $z_{\rm phot} = 1.10^{+0.02}_{0.00}$ and $z_{\rm spec} = 0.892 \pm 0.001$; COSMOS 0018+3845: $z_{\rm phot} = 0.44 \pm 0.01$

Table 2. Position and redshift of galaxies in the FORS1 field around COSMOS 0012+2015, COSMOS 0013+2249, and COSMOS 0049+5128. The error on the redshifts is ±0.001.

RA	Dec	z
COSMOS 0012+2015		
150.01554	2.3105342	0.492
150.05263	2.3377222	0.378
150.07391	2.3256596	0.222
150.07463	2.3485102	0.217
150.07239	2.3679651	0.344
150.08564	2.3641732	0.340
150.10210	2.3524922	0.220
150.11477	2.3328146	0.373
COSMOS 0013+2249		
150.10193	2.3900368	0.218
150.09001	2.3836205	0.530
150.08210	2.3904710	0.351
150.07843	2.3895686	0.352
150.07239	2.3679506	0.347
150.06510	2.3855444	0.343
150.05808	2.3804333	0.346
150.05235	2.3837337	0.350
150.03149	2.3745112	0.220
150.02774	2.3738948	0.222
150.00332	2.4075260	0.347
COSMOS 0049+5128		
150.23256	1.8862956	0.673
150.23365	1.8704970	0.283
150.21829	1.8847159	0.621
150.20779	1.8823028	0.026
150.20824	1.8753444	1.146
150.20526	1.8578028	0.337
150.19758	1.8606685	0.267
150.18165	1.8552841	0.168

and $z_{\rm spec} = 0.9755 \pm 0.0003$). In those three cases, the photometry of the lens galaxy obtained from ground-based data is contaminated by the close and bright images of the source, and the photometric redshift determination is consequently biased.

2.3. Stellar masses of the lens galaxies

We derived a first set of stellar masses using the Bayesian code described in Bundy et al. (2006). In brief, a data couple, made of the observed galaxy spectral energy distribution (SED) and its redshift, is referenced to a grid of models that are constructed with the Bruzual & Charlot (2003) synthesis code. The grid includes models that vary in age, star-formation history, dust content and metallicity. At each grid point, the probability that the observed SED fits the model is calculated: the corresponding stellar mass and the stellar mass-to-K-band luminosity ratio are stored. By minimizing over all parameters in the grid, the stellar mass probability distribution is obtained. The median of this distribution is taken as the stellar mass estimate, while the width corresponding to 68% of the probability distribution encodes the error bar that results from degeneracies and uncertainties in the model parameter space. The final error bar on the stellar mass also includes the K-band photometric uncertainty and the expected error on the luminosity distance that results from the uncertainty on the photometric redshift. The stellar masses and uncertainties are provided in Table 3 and plotted in Fig. 4.

From the ACS-F814W images (Koekemoer et al. 2007) we infer the contamination from the light of the background-lensed images in the stellar mass measurements. In an aperture of 3″ radius, the lensed images are 3 to 7 mag fainter than their respective lensing galaxy: in all cases this contamination generates an error on the stellar mass $\lesssim$0.01 dex.

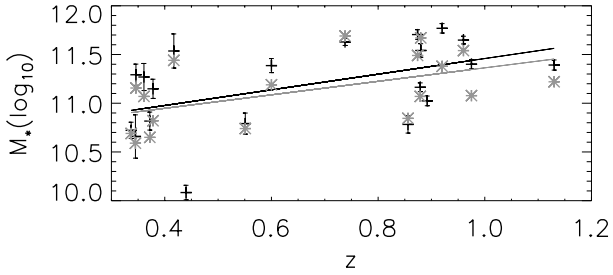

Fig. 4. Stellar masses (in $M_\odot$) of the lens galaxies as a function of redshift (spectroscopic when available, photometric otherwise). Black crosses: stellar masses inferred using the method described in Bundy et al. (2006). Grey stars: stellar masses inferred for the IRAC sources in Ilbert et al. (2010). Black and grey lines: the respective least-square fits, with a slope of +0.8 ± 0.3 (black line) and +0.7 ± 0.3 (grey line).

To estimate the reliability of our estimates of the stellar mass (and uncertainties), we retrieved among the 3.6μ IRAC catalog of the Spitzer-COSMOS survey (Sanders et al. 2007) 18 of the 20 strong-lenses; the other two lens galaxies were not detected with Spitzer. For these lenses we compared our estimates of the stellar masses to those inferred by Ilbert et al. (2010[2]): they agree reasonably well (see Fig. 4). The typical difference between the two mass estimators (∼0.2 dex) is widely discussed in Ilbert et al. (2010). Both distributions show a tendency of increasing the lens stellar mass with redshift. We will return to this feature in more detail in the discussion (Sect. 5.1).

3. The environment of the lens galaxies

With these more accurate redshift measurements for the lens galaxies and the galaxies in the COSMOS field, we can undertake a study of the local environments of lens galaxies. Indeed, to understand whether high-redshift lensing galaxies ($z \geq 0.3$) are representative of the ETG population at their redshift, as the low-redshift lens galaxies are (T09, Auger 2008), we study their environment in comparison to the environment of a population of non-lensing ETGs. Our first analysis of the lens environment with regard to LSS (Paper II) led to the conclusion that lens galaxies are indeed evolving in the same environment as their parent population. Let us now look closer at a more local environment for the lens, using neighbor density measurements as defined and used by T09 for the SLACS sample.

3.1. Projected number of neighbors

3.1.1. The neighbor number densities

In T09, the first estimator is the projected number density of galaxies, Σ_{10}, inside a circle with radius R_{10}, which is equal to the projected distance to the ninth closest neighbor of the lens. The neighbor galaxies are defined in a way that their magnitude is: $i^+ < i^+_{\rm lens} + 3$, and the upper or lower bound, z, of their photometric redshift is $z_{\rm lens} - \delta z_{\rm lens} < z < z_{\rm lens} + \delta z_{\rm lens}$, where $\delta z_{\rm lens}$ is a function of the lens magnitude and redshift, and lies between 0.012 and 0.020 for our sample (see Ilbert et al. 2009). For the two lenses with incorrect photometric redshifts, we used their spectroscopic redshift instead and for the search for neighbors, the $\delta z_{\rm lens}$ values associated with their spectroscopic redshift in the photometric catalog; this ensures that we are using the same

[2] The COSMOS catalogs can be found at http://irsa.ipac.caltech.edu/data/cosmos

Table 3. Summary of the properties of the lens galaxy environments (top to bottom: from low to high redshift).

Name	z lens/source	$i^+ \pm \delta i^+$	$\frac{\Sigma_{10}}{\langle\Sigma_{10}\rangle_t}$	R_{10} kpc	$\frac{D_1}{\langle D_1\rangle_t}$	N_1	$M_\star$ log10() $M_\odot$	$N_{\rm twin}$
COSMOS 0049+5128	0.337 ± 0.001	20.32 ± 0.01	1.3 ± 1.9	1013	1.0 ± 0.9	10	10.72 ± 0.08	63
COSMOS 5947+4752	0.345 ± 0.001	20.36 ± 0.01	1.9 ± 1.5	947	1.6 ± 0.7	13	10.65 ± 0.22	59
COSMOS 0013+2249	0.346 ± 0.001	19.63 ± 0.01	6.2 ± 0.2	602	2.3 ± 0.5	16	11.29 ± 0.10	23
COSMOS 0056+1226	0.361 ± 0.001/0.808 ± 0.001	19.77 ± 0.01	1.4 ± 1.2	996	1.1 ± 0.7	11	11.26 ± 0.13	42
COSMOS 5857+5949	0.372 ± 0.001	20.55 ± 0.01	0.9 ± 4.5	1348	0.4 ± 2.2	5	10.81 ± 0.09	69
COSMOS 0012+2015	0.378 ± 0.001	19.95 ± 0.01	1.9 ± 1.1	833	1.1 ± 0.7	12	11.14 ± 0.09	40
COSMOS 0254+1430	0.417 ± 0.001/0.779 ± 0.001	19.76 ± 0.01	0.5 ± 3.5	1767	0.6 ± 1.1	5	11.53 ± 0.17	28
COSMOS 5921+0638	0.551 ± 0.001/3.14 ± 0.05	20.82 ± 0.01	0.6 ± 4.1	1939	0.4 ± 1.6	3	10.79 ± 0.10	51
COSMOS 0216+2955	0.608 ± 0.001	20.71 ± 0.01	4.6 ± 0.3	665	2.7 ± 0.3	19	11.38 ± 0.07	29
COSMOS 0038+4133	0.738 ± 0.001	21.03 ± 0.01	5.5 ± 0.9	585	1.9 ± 0.5	17	11.62 ± 0.03	30
COSMOS 0124+5121	0.856 ± 0.001	22.61 ± 0.02	2.9 ± 1.0	777	2.1 ± 0.4	15	10.78 ± 0.08	140
COSMOS 0047+5023	0.87 ± 0.01	21.35 ± 0.01	2.3 ± 4.8	851	1.3 ± 0.7	11	11.70 ± 0.04	22
J100140.12+020040.9	0.879 ± 0.001	22.01 ± 0.01	0.6 ± 4.7	1931	0.3 ± 2.6	2	11.16 ± 0.04	94
COSMOS 5941+3628	0.88 ± 0.01	21.60 ± 0.01	2.5 ± 0.4	946	2.0 ± 0.3	12	11.54 ± 0.06	39
J095930.93+023427.7	0.892 ± 0.001	21.98 ± 0.01	1.2 ± 2.4	1131	0.8 ± 0.9	7	11.02 ± 0.05	92
COSMOS 0211+1139	0.92 ± 0.01	21.65 ± 0.01	1.8 ± 0.6	948	1.6 ± 0.4	13	11.76 ± 0.04	31
COSMOS 0050+4901	0.960 ± 0.001	22.01 ± 0.01	0.8 ± 4.9	1735	0.6 ± 1.5	4	11.64 ± 0.03	43
COSMOS 0227+0451	0.975 ± 0.001	22.09 ± 0.01	0.5 ± 6.8	2149	1.0 ± 0.9	7	11.39 ± 0.04	58
COSMOS 0018+3845	0.9755 ± 0.0003/3.96 ± 0.02	23.43 ± 0.03	1.0 ± 1.3	1799	0.3 ± 1.2	5	10.73 ± 0.06	119
COSMOS 5914+1219	1.13 ± 0.10	23.00 ± 0.02	0.9 ± 0.3	1832	0.7 ± 1.2	3	11.39 ± 0.05	45

Notes. (1) Lens name. (2) Redshifts of the lensing galaxies, followed by that of the source when known. (3) Subaru i^+ magnitude. (4), (6) Number density ratios measured as explained in Sect. 3.1. (5) Radius encompassing the 9th closest neighbor. (7) Total number of galaxies within 1 Mpc from the lens. (8) Lens galaxy stellar mass. (9) Number of twins in the photometric catalog of Ilbert et al. (2010).

search box for lenses with spectroscopic and photometric redshifts.

The search for neighbors is performed in the photometric redshift catalog of Ilbert et al. (2009), which contains about one million objects. The limiting magnitude chosen for the neighbors ensures that the scaling in brightness (thus in mass) between a lens galaxy and its neighbors is the same for all lenses, independently of their magnitude. For the faintest lens in our sample, this upper limit corresponds to the completeness limit of the COSMOS photometric catalog (depth: $i^+ \sim 26.2$, Capak et al. 2007a). The range chosen for the redshift ensures that, given the error bars on the neighbor photometric redshifts, they are indeed at the same redshift as the lens galaxies (in the 68% confidence limit error bars).

As in T09, we also computed the projected number of galaxies, D_1, inside a circle with radius 1 Mpc, at the lens redshift. To select the neighbors, we used the same limiting magnitudes and redshift ranges as for the first estimator.

To achieve comparative measurements for a population of galaxies that are not identified as lenses but have the same morphology (early photometric type), similar brightness and redshift properties, we defined a control sample of "twins" for each lens galaxy. Those twins have the upper or lower bounds, $z_{\rm twin}$, of their photometric redshift in a way that $z_{\rm lens} - \delta z < z_{\rm twin} < z_{\rm lens} + \delta z$ with $\delta z = 0.05$, and the upper or lower bounds, $I_{\rm twin}$, of their magnitude such as: $I_{\rm lens} - \delta I < I_{\rm twin} < I_{\rm lens} - \delta I$, with $\delta I = 0.05$ mag. The dispersion authorized around the value of the lens redshift and lens magnitude ensures that the sample of twins is large enough for the results to be statistically reliable (between 22 and 140 twins, see Table 3). In addition, the range in redshift is small enough to avoid possible biases owing to galaxy evolution, and the range in magnitude ensures that the flux difference between a lens and its twins remains lower than 5%. We then measure the average number density of neighbors $\langle\Sigma_{10}\rangle_t$ and the average projected number of galaxies in a circle with radius 1 Mpc: $\langle D_1\rangle_t$ for the control "twin" sample.

For an obvious lack of spectroscopic information, the twins cannot be selected according to their velocity dispersion as it is the case in the analysis by T09. Yet our match in magnitude and redshift mimics up to a certain level of accuracy a match in mass between the lens galaxies and their twins.

3.1.2. Error measurements on the neighbor number densities

In building the photometric catalog of galaxies, masks were necessary to hide bright objects disturbing the galaxy extraction procedure (see Capak et al. 2007a). From these masks we measured at each lens and twin location, the surface that was hidden for the extraction. The hidden surface is typically of a few percents of the total surface used to determine Σ_{10} or D_1. It only gives a positive contribution to the total error budget on the neighbor density estimates: indeed, the surface covered by the circle of radius R_{10} would be smaller if the ninth closest galaxy were behind the mask, and if one or more galaxies were hidden behind the mask, the number of galaxies in a circle of radius D_1 would be larger. Therefore, for a fixed number of galaxies, the surface has to be smaller. In summary, for a lens galaxy the total error bar on the neighbor galaxy density is the quadratic sum of the Poisson error and the error owing to the use of masks on the surface encompassing the neighbors. For its average twin, the error bar is the quadratic sum of the Poisson error, the error owing to the use of masks and the dispersion for the population of twins. The Poisson error largely dominates the error budget for the lens neighbor number densities, while the dispersion largely dominates the error budget for the twins.

3.1.3. Results

The values of Σ_{10}, D_1, $\langle\Sigma_{10}\rangle_t$ and $\langle D_1\rangle_t$ depend on the redshift bin and magnitude limit. To circumvent these effects, we only

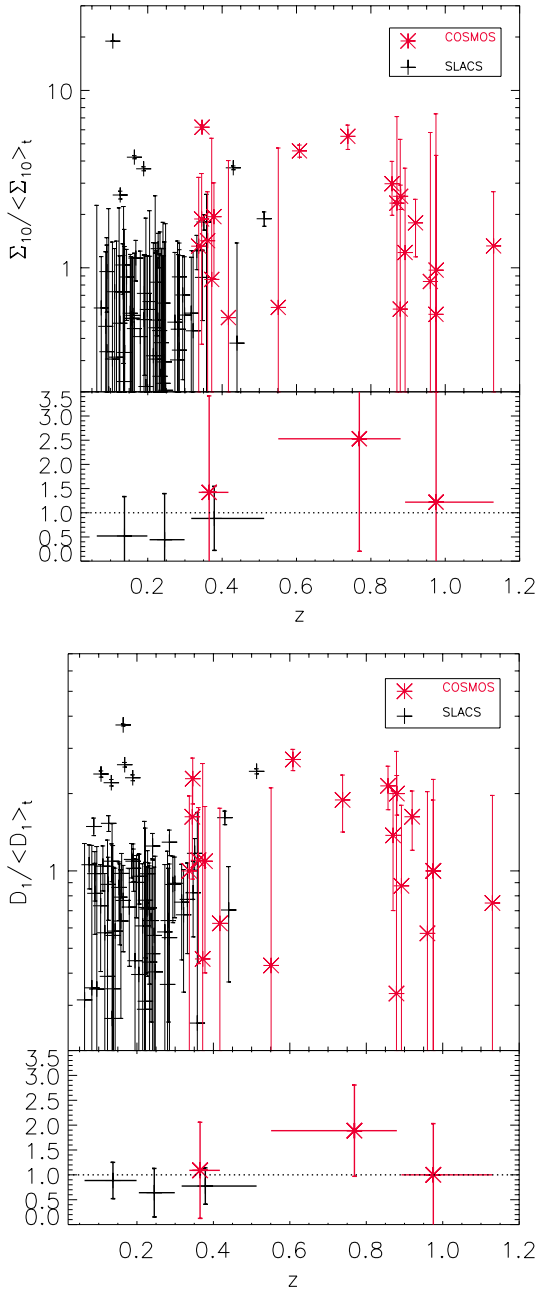

Fig. 5. Distribution of $\frac{\Sigma_{10}}{\langle\Sigma_{10}\rangle_t}$ (*top plot*) and $\frac{D_1}{\langle D_1\rangle_t}$ (*bottom plot*) as a function of the lens redshift for the COSMOS lenses (red stars) and the SLACS lenses (black crosses). In each plot, the lower panel displays a re-binned version of the upper plot using the the median of the ratios in different bins (SLACS bins: $z < 0.2$ (32 galaxies), $0.2 \leq z < 0.3$ (23 galaxies), $0.3 \leq z < 0.5$ (9 galaxies); COSMOS bins: $0.30 \leq z < 0.42$ (7 galaxies), $0.42 \leq z < 0.89$ (7 galaxies), $0.89 \leq z < 1.30$ (6 galaxies).

interpret the results in term of ratios: $\frac{\Sigma_{10}}{\langle\Sigma_{10}\rangle_t}$ and $\frac{D_1}{\langle D_1\rangle_t}$. These ratios quantify the richness of the environment of the lens galaxies in comparison to the environment of their respective twins. They are provided in Table 3. The average distance encompassing the nine closest galaxies to the lens is $\langle R_{10}\rangle = 1.2$ Mpc with a 1σ standard deviation of 0.5 Mpc, hence comparable to the radius of 1 Mpc used to calculate D_1. In Fig. 5, we display the ratios $\frac{\Sigma_{10}}{\langle\Sigma_{10}\rangle_t}$ and $\frac{D_1}{\langle D_1\rangle_t}$ for the COSMOS lenses and for the SLACS lenses (using data from T09), as a function of redshift. A priori, the two distributions cannot be directly compared because they may have different normalization factors (because of their different lens selection function, source redshift distribution and survey sensitivity). Yet, in the redshift range common to the SLACS and COSMOS samples ($z \sim [0.33, 0.50]$), the levels of the distributions for $\frac{\Sigma_{10}}{\langle\Sigma_{10}\rangle_t}$ and $\frac{D_1}{\langle D_1\rangle_t}$ are similar, which suggests that the normalizations are not drastically different. However, to avoid any misinterpretation deriving from intrinsic sample differences, the SLACS sample and the COSMOS sample distributions are separately analyzed.

The number density ratios displayed in Fig. 5 indicate whether the lens galaxies reside in a typical environment compared to the twin galaxy population. If this were true, the number density ratios should be on the order of 1 at every redshift. This is indeed the case on average for the lenses in the redshift range studied here.

3.2. X-ray and optically detected galaxy groups and clusters

The validity of the estimators used to characterize the environments of lens galaxies in Sect. 3.1 can be checked using the distribution of groups and clusters in the field based on X-ray and spectroscopic data analysis. Indeed, we can access two supplementary pieces of information: (a) the distribution of X-ray emitting gas in the COSMOS field (XMM-Newton survey: Hasinger et al. 2007; and C-COSMOS with Chandra: Elvis et al. 2009), which traces galaxy groups and clusters in the field (Finoguenov et al. 2007, and in prep.), and (b) the identification of optical groups or clusters (Knobel et al. 2009) from the z-COSMOS spectroscopic program (Lilly et al. 2007).

Moreover, because the presence of groups in the direction toward the source generates a different lensing potential compared to that of a single lens galaxy, it is important in preparation of the mass modeling in Sect. 4 to know: 1) if the lens galaxies are group members. If this is indeed the case, the group has to be modeled as an individual potential in the lens modeling; 2) which contribution in terms of shear is produced by the groups and clusters toward and around the lens galaxy. Most of the time this contribution is simply represented by an "external shear" whose parameters are optimized while adjusting the lens model. In this paper, we instead intend to independently measure the external shear using the rich dataset that covers the COSMOS field, in a similar manner than what has been done recently by Wong et al. (2011).

In the framework of our lensing analysis, each of the group catalogs (X-ray-selected versus spectroscopically selected) has certain advantages and disadvantages. The entire COSMOS region has been mapped through 54 overlapping XMM-Newton pointings while additional Chandra observations have mapped the central region (0.9 square degrees). A composite XMM-Newton and Chandra mosaic has been used to detect and measure the fluxes of groups and clusters to a 4σ detection limit of 1.0×10^{-15} erg cm^{-2} s^{-1} over 96% of the ACS field. The general data reduction process can be found in Finoguenov et al. (2007, 2009) and the cluster catalog and weak-lensing analysis are presented in Leauthaud et al. (2010). Therefore, the catalog of X-ray selected groups and clusters is homogeneous and covers the entire COSMOS field. However, it is affected by the sensitivity threshold of the X-ray survey, which is different from the sensitivity cut of the optical dataset. Therefore, groups of modest mass could be missing from the X-ray selected catalog, especially around galaxies at high redshift.

Conversely, the catalog of optically selected groups in COSMOS has the advantage of spanning the same brightness

Table 4. Summary of the contribution of the environment to the lens galaxies.

Name	P	N	κ	γ	PA_γ	Cluster	Dist.
					deg	ID ($z \pm \delta z$, log10(M_{200}), c, r_{200})	kpc
COSMOS 0049+5128	0.33	13	$0.006 \pm 0.001^{+0.000}_{-0.001}$	$0.008 \pm 0.003^{+0.001}_{-0.001}$	$-38 \pm 12^{+0}_{-1}$	–	–
COSMOS 5947+4752	0.04	3	$0.016 \pm 0.003^{+0.006}_{-0.001}$	$0.021 \pm 0.005^{+0.008}_{-0.006}$	$0 \pm 2^{+0}_{-3}$	–	–
COSMOS 0013+2249	0.33	26	$0.023 \pm 0.003^{+0.000}_{-0.008}$	$0.025 \pm 0.005^{+0.001}_{-0.002}$	$8 \pm 10^{+1}_{-1}$	#173 (0.348 ± 0.005, 13.44, 4.18, 0.55)	0.5
COSMOS 0056+1226	0.76	29	$0.011 \pm 0.003^{+0.000}_{-0.000}$	$0.003 \pm 0.004^{+0.000}_{-0.000}$	$-18 \pm 30^{+0}_{-0}$	#133 (0.360 ± 0.005, 13.28, 4.32, 0.48)	0.3
COSMOS 5857+5949	0.58	18	$0.019 \pm 0.005^{+0.002}_{-0.003}$	$0.033 \pm 0.010^{+0.005}_{-0.004}$	$-41 \pm 8^{+0}_{-0}$	–	–
COSMOS 0012+2015	0.39	31	$0.019 \pm 0.002^{+0.000}_{-0.003}$	$0.009 \pm 0.006^{+0.000}_{-0.001}$	$-24 \pm 19^{+5}_{-0}$	–	–
COSMOS 0254+1430	0	2	$0.002 \pm 0.000^{+0.000}_{-0.000}$	$0.006 \pm 0.000^{+0.000}_{-0.000}$	$-31 \pm 3^{+0}_{-0}$	–	–
COSMOS 5921+0638	0.61	24	$0.019 \pm 0.004^{+0.000}_{-0.000}$	$0.009 \pm 0.012^{+0.000}_{-0.000}$	$-37 \pm 31^{+0}_{-0}$	–	–
COSMOS 0216+2955	0.06	5	$0.025 \pm 0.003^{+0.005}_{-0.005}$	$0.024 \pm 0.004^{+0.000}_{-0.003}$	$36 \pm 5^{+3}_{-4}$	#221 (0.600 ± 0.005, 13.56, 3.82, 0.55)	0.2
COSMOS 0038+4133	0.12	4	$0.004 \pm 0.000^{+0.001}_{-0.001}$	$0.014 \pm 0.002^{+0.004}_{-0.003}$	$-4 \pm 4^{+2}_{-0}$	–	–
COSMOS 0124+5121	0.20	2	$0.002 \pm 0.000^{+0.001}_{-0.001}$	$0.007 \pm 0.002^{+0.000}_{-0.000}$	$9 \pm 3^{+2}_{-0}$	–	–
COSMOS 0047+5023	0.06	4	$0.012 \pm 0.002^{+0.002}_{-0.002}$	$0.016 \pm 0.003^{+0.004}_{-0.003}$	$-26 \pm 6^{+0}_{-0}$	–	–
J100140.12+020040.9	0.20	3	$0.006 \pm 0.001^{+0.001}_{-0.000}$	$0.009 \pm 0.002^{+0.001}_{-0.001}$	$-28 \pm 7^{+0}_{-0}$	–	–
COSMOS 5941+3628	0.07	7	$0.024 \pm 0.003^{+0.004}_{-0.005}$	$0.007 \pm 0.004^{+0.010}_{-0.004}$	$22 \pm 15^{+9}_{-1}$	–	–
J095930.93+023427.7	0.27	4	$0.006 \pm 0.001^{+0.002}_{-0.001}$	$0.016 \pm 0.004^{+0.002}_{-0.001}$	-45 ± 1	#288 (0.697 ± 0.006, 13.63, 3.73, 0.56)	102
COSMOS 0211+1139	0	3	$0.004 \pm 0.000^{+0.001}_{-0.001}$	$0.022 \pm 0.005^{+0.006}_{-0.005}$	$43 \pm 3^{+0}_{-1}$	–	–
COSMOS 0050+4901	0.25	2	$0.001 \pm 0.000^{+0.001}_{-0.000}$	$0.006 \pm 0.001^{+0.001}_{-0.001}$	$-16 \pm 4^{+5}_{-3}$	–	–
COSMOS 0227+0451	0	4	$0.002 \pm 0.000^{+0.001}_{-0.001}$	$0.005 \pm 0.001^{+0.002}_{-0.002}$	$-19 \pm 6^{+4}_{-9}$	# 101 (0.98 ± 0.01, 13.70, 3.65, 0.53)	0.5
COSMOS 0018+3845	0.38	15	$0.037 \pm 0.007^{+0.000}_{-0.000}$	$0.082 \pm 0.016^{+0.000}_{-0.000}$	$13 \pm 4^{+0}_{-0}$	–	–
COSMOS 5914+1219	0.25	17	$0.001 \pm 0.000^{+0.000}_{-0.000}$	$0.006 \pm 0.001^{+0.000}_{-0.000}$	$-19 \pm 5^{+1}_{-0}$	–	–

Notes. (1) Lens name. (2) Probability that galaxies in a $2' \times 2'$ field around the lens galaxy are included in the z-COSMOS catalog. (3) The number of groups involved in the calculation of the external shear (within $5'$ projected radius). (4–6) Convergence, shear strength, and shear direction of the groups and clusters around the lens. The first set of errors comes from the uncertainty on the group mass. The second set of errors comes from the uncertainty on the source redshift, which was chosen to be ±0.5 for sources with unknown redshifts and the error on the source redshift estimation from Table 3, when it was measured. (7) The ID of the group or cluster with an impact parameter smaller than its radius (r_{200}) in Leauthaud et al. (2010). In parenthesis are its redshift, mass (in solar mass), concentration, and radius (in Mpc). The error on the cluster mass is 40% of the total mass (Vikhlinin et al. 2009). (8) Projected distance in kpc between the lens and the group/cluster center (at the lens redshift).

range as the optical imaging dataset from which the strong-lens candidates and the arcs were extracted. Even though the faintest galaxies seen on deep images will remain undetected in the shallower spectroscopic z-COSMOS survey, groups can still be traced and assessed from their central brightest galaxies. Then, the parameters of the galaxy groups can be derived by comparing these detections to a catalog of mock-groups that are subject to the same detection criteria (see Knobel et al. 2009, for an extensive description of the group catalog). The first data release of the z-COSMOS survey (Lilly et al. 2007) covers a fraction of the full COSMOS field, which leaves some of our COSMOS lens candidates outside the coverage of the group catalog.

Let us establish now whether the lens galaxies are group or cluster members (Sect. 3.2.1) and measure the external shear contribution of the groups and clusters at the lens galaxy position (Sect. 3.2.3).

3.2.1. Lens galaxy group members

We cross-correlated the X-ray cluster catalog (Leauthaud et al. 2010) with the sample of strong-lenses. We defined as a group member a lens galaxy located within r_{200} (radius where the matter density is 200 times the critical density) of the group center, and with a redshift identical to the group redshift (within error bars). We found four matches, and there is a galaxy cluster detected at a lower redshift in direction to J095930.93+023427.7 (see Table 4).

Using the group catalog built from the optical dataset, we did not identify any new groups associated in redshift and space with lens galaxies tin addition to those already identified with the X-ray catalog. In Table 4 we give the probability that galaxies in a $2' \times 2'$ field around the lens galaxy are included in the z-COSMOS catalog. This figure roughly establishes the "completeness" of the survey at every lens location and tells us if the z-COSMOS group catalog can be used to characterize the environment of the lens.

3.2.2. Comparison: galaxy group members and projected number density of neighbors

In principle, lens galaxies that are group members are expected to have large neighbor number densities. This should be visible in the ratio measured in Sect. 3.1. This is indeed the case with the first estimator for the lens in COSMOS 0013+2249 ($\frac{\Sigma_{10}}{\langle\Sigma_{10}\rangle_t} = 6.2 \pm 0.2$) and COSMOS 0216+2955 ($\frac{\Sigma_{10}}{\langle\Sigma_{10}\rangle_t} = 4.6 \pm 0.3$), and it is unclear for COSMOS 0056+1226 and COSMOS 0227+0451 because of the large error bar on the measured density ratios. With the second estimator, the ratio is in average lower than with $\frac{\Sigma_{10}}{\langle\Sigma_{10}\rangle_t}$, and it is therefore more difficult to correctly identify an

over-dense field. On the contrary, COSMOS 0038+4133 shows a high density ratio ($\frac{\Sigma_{10}}{\langle\Sigma_{10}\rangle_t} = 5.5 \pm 0.9$) without being associated to any known galaxy group in X-ray or optic.

3.2.3. The external shear produced by clusters and groups

We estimate the shear and convergence produced by the groups (either X-ray or optical) that is detected around the lens galaxies in order to characterize the contribution of the environment to the total lens potential in future lens models (Sect. 4). To do so we followed the method described in Paper III. In short, we computed the convergence and shear produced by all groups closer in projection than a given radius (5′, as in Paper III), and at any redshift up to that of the source. We assume that the mass profile of every group follows a truncated isothermal sphere (TIS). The choice of this profile is motivated by the fact that the shear and convergence produced by an isothermal sphere are easy to compute (Keeton 2003; Momcheva et al. 2006). Moreover, because we will consider only groups and clusters that do not cross the line-of-sight to the source, estimations of their total masses instead of their mass distributions are sufficient for the accuracy of the result. We selected a truncated profile to avoid to give unrealistically much weight to the most distant groups.

The three-dimensional density distribution of the TIS can be written

$$\rho \propto \frac{1}{r^2}\frac{1}{r^2 + r_c^2}, \tag{1}$$

where r_c is the truncation radius. The convergence, κ, and shear, γ, produced by this profile are respectively

$$\kappa = \frac{\tilde{b}}{2}\left(\frac{1}{\sqrt{r^2}} - \frac{1}{\sqrt{r_c^2 + r^2}}\right) \tag{2}$$

$$\gamma = \frac{\tilde{b}}{2}\left[\frac{1}{\sqrt{r^2}} + \frac{1}{\sqrt{r_c^2 + r^2}} - \frac{2r_c}{r^2}\left(\frac{\sqrt{r_c^2 + r^2}}{r_c} - 1\right)\right], \tag{3}$$

where $\tilde{b}$ is the impact parameter of the TIS, which relates to the singular isothermal sphere (SIS) impact parameter b_{SIS} as

$$\frac{b_{SIS}}{\tilde{b}} = 1 + \frac{r_c}{b_{SIS}} - \sqrt{1 + \left(\frac{r_c}{b_{SIS}}\right)^2}. \tag{4}$$

In the limit where $r_c \to \infty$ these quantities match those of the SIS.

To compute the external shear produceded by the groups and clusters we proceed as follows. Whenever $P < 0.3$ in Table 4 (Col. 2), we only considered the catalog of X-ray-detected groups and clusters. The group's mass potentials are modeled as TIS using the value M_{200} and r_{200} (used as the truncature radius). The error on the X-ray mass comes from the scatter in the relation that is used to derive the mass from the luminosity (Leautaud et al. 2010): it is on the order of ±20% of M_{200} (Vikhlinin et al. 2009). Whenever $P \geq 0.3$ in Table 4 (Col. 2), we also considered the optical group catalog in addition to the X-ray group catalog. We first correlated the optical and X-ray group catalogs to identify and remove optical groups that might already be accounted for as an X-ray group. Then, we modeled as TIS the remaining optical groups using the "mock" virial mass, M_{vir}, and the "mock" virial radius, r_{vir} (used as the truncature radius). The upper and lower error on the virial mass are $^{+100\%}_{-50\%}$ of M_{vir} (Knobel et al. 2009). These "mock" quantities are the theoretical values associated with the detected groups when subjecting a mock sample of groups to the same selection function and same survey criteria as the observations (see Knobel et al. 2009, for details).

The external shear and associated convergence are calculated individually for each group. They are then re-scaled to the redshift of the lens with the scaling relation given in Momcheva et al. (2006). For a given lens, external shear and convergence are summed following the procedure described in Keeton (2003) and Momcheva et al. (2006). The results are summarized in Table 4. A first set of errors on the shear and on the convergence results from the propagation of the group mass errors.

As mentioned already, in the special case where a galaxy group or cluster has an impact parameter smaller than r_{200} or r_{vir} (in 5 cases, see Table 4), the shear and convergence calculated under this simple approximation are incorrect (Keeton 2003). Hence, we systematically removed these groups when computing the external shear. Instead, they will have to be accounted for as additional lens potential when we perform the lens modeling.

Regarding the source redshift, it is either known spectroscopically for some lenses (see Table 3), or assumed to be at $z_s = 2$ for lenses with $z_l < 1$, or at $z_s = 3$ for lenses with $z_l > 1$. The convergence and shear contributions depend on the number of groups taken into account, which in turn may depend on the source redshift and on the considered cut-radius. Hence, an error on the source redshift generates an error on the external shear parameter. We estimated this error assuming an uncertainty $\delta z = \pm 0.5$ on the source redshift when unknown, and using the error on the source redshift in Table 3 when measured (see Table 4). To estimate the error introduced by an arbitrary cut-radius at 5′, we also probed two other radii (7′ and 10′). We found that the incidence of the radius selection on the final lensing contribution is $\delta\kappa \sim \delta\gamma \sim 0.001$ and is negligible on the orientation of the shear ($\delta PA_\gamma < 0.5°$). Then we calculated the total error on the external shear as the sum in quadrature of the error produced by the group mass uncertainty, the source redshift uncertainty, and the error produced by the choice of aperture.

We also analyzed the error on the external shear parameters generated when using a single catalog of groups (X-ray) instead of the combination of the two catalogs (X-ray and optical). The comparison is possible for seven systems. While the convergence is different when using a single catalog instead of two, the external shear strength and direction agree within their respective error bars. This means that our calculation realistically associates the largest source of shear with the more massive groups and clusters. It also means that the probable incompleteness of our catalogs in low-mass groups has a minimal impact on the shear measurement: what matters is the completeness of the catalog in large mass groups and clusters. However, the technique is limited for low-redshift sources, because there is no X-ray cluster detected above $z = 1.3$ in the COSMOS field.

4. The strong-lens modeling

In this section, we focus on the 12 lens galaxies that offer the largest number of observational constraints: the triple and quadruple image systems and the Einstein rings.

4.1. Lens-galaxy light profiles

We re-computed the two-dimensional fit of the galaxy surface brightness distribution of the COSMOS lenses using GIM2D (Simard 1998; Marleau & Simard 1998) to include error bars that were not presented in Paper I. For that purpose, we adopt as in Paper I a Sersic bulge plus an exponential disk parametrization to

Table 5. Lens galaxy luminous profile.

Name	Sersic parameters				
	ϵ	PA	R_e	R_e	n
		deg	kpc	$''$	
COSMOS 0049+5128	$0.22^{+0.00}_{-0.01}$	-25^{+1}_{-1}	$5.15^{+0.04}_{-0.03}$	$1.10^{+0.01}_{-0.01}$	$1.19^{+0.01}_{-0.02}$
COSMOS 5947+4752	$0.05^{+0.15}_{-0.05}$	4^{+7}_{-16}	$2.49^{+1.53}_{-0.54}$	$0.52^{+0.32}_{-0.11}$	$1.38^{+0.53}_{-0.36}$
COSMOS 5921+0638	$0.14^{+0.06}_{-0.03}$	97^{+18}_{-8}	$2.88^{+3.37}_{-0.11}$	$0.46^{+0.54}_{-0.02}$	$1.00^{+1.35}_{-0.04}$
COSMOS 0038+4133	$0.25^{+0.08}_{-0.09}$	-3^{+26}_{-4}	$5.25^{+0.81}_{-2.37}$	$0.74^{+0.11}_{-0.33}$	$4.30^{+0.50}_{-1.00}$
COSMOS 0124+5121	$0.23^{+0.16}_{-0.03}$	-52^{+28}_{-4}	$1.82^{+0.15}_{-0.17}$	$0.24^{+0.02}_{-0.02}$	$1.89^{+0.29}_{-0.14}$
COSMOS 0047+5023	$0.19^{+0.01}_{-0.01}$	33^{+2}_{-2}	$5.40^{+0.10}_{-0.08}$	$0.72^{+0.01}_{-0.01}$	$1.25^{+0.03}_{-0.03}$
J100140.12+020040.9	$0.16^{+0.06}_{-0.02}$	21^{+8}_{-6}	$2.42^{+0.22}_{-0.52}$	$0.32^{+0.03}_{-0.07}$	$2.59^{+0.13}_{-0.23}$
COSMOS 5941+3628	$0.24^{+0.10}_{-0.16}$	-5^{+22}_{-17}	$5.89^{+0.22}_{-0.24}$	$0.78^{+0.03}_{-0.03}$	$1.18^{+0.36}_{-0.10}$
J095930.93+023427.7	$0.21^{+0.05}_{-0.05}$	-77^{+6}_{-7}	$1.62^{+0.50}_{-0.68}$	$0.21^{+0.07}_{-0.09}$	$1.90^{+0.34}_{-0.79}$
COSMOS 0050+4901	$0.30^{+0.06}_{-0.03}$	27^{+3}_{-10}	$2.85^{+0.47}_{-1.00}$	$0.37^{+0.06}_{-0.13}$	$5.58^{+0.19}_{-0.13}$
COSMOS 0018+3845	$0.22^{+0.00}_{-0.01}$	-22^{+1}_{-1}	$2.32^{+0.54}_{-1.31}$	$0.30^{+0.07}_{-0.17}$	$5.60^{+0.19}_{-0.13}$
COSMOS 5914+1219	$0.13^{+0.02}_{-0.10}$	14^{+48}_{-2}	$2.21^{+0.06}_{-1.15}$	$0.27^{+0.01}_{-0.13}$	$1.40^{+2.28}_{-0.06}$

Notes. (1) Lens name. Parameters of the Sersic light profile fit: (2) ellipticity, (3) position angle, (4) effective radius in kpc and (5) in arcsec and (6) index, with associated error bars (from GIM2D, 68% confidence limit).

describe the two-dimensional surface brightness distribution of the lens galaxy light profile. The Sersic profile is parametrized by means of the total flux in the bulge, the Sersic index, n, the bulge ellipticity, $\epsilon = 1 - b/a$, the position angle of the bulge, PA, and the effective radius of the bulge, R_e. The exponential profile depends on the photometric disk total flux, the disk scale-length, the disk position angle and the disc inclination. The software gives the best-fitting values for all these parameters. The parameters of the Sersic bulges are summarized in Table 5. The error bars correspond to the 68% confidence level. For most systems, the results are consistent with the surface brightness parameters measured in Paper I. But for others, such as COSMOS 5921+0638, the best-fit parameters differe in Paper I, Paper III, and here. Indeed, the presence of a ring or bright arcs close to the lens galaxy center impide producing a robust fit of the lens-galaxy surface brightness density profile; this is true even when more complex fitting and deconvolution methods are used (see Chantry & Magain 2007).

The relative image positions to the lens galaxies are the main constraints for the lens models. For images that are point like objects, the determination of their positions only depends on the image resolution. This is the case for COSMOS 5921+0638. For this system the error on the relative position is 0.014″ (see Paper III). For the other multiple images systems, we determine the position of the the brightest peak in each image. For theses systems, the error on the relative position of the images is typically 0.05″. For the perfect rings that do not display any peak we place the image arbitrarily around the ring in a symmetric way around the lens center and assume that the error on the relative position of the images is 0.05″. In Table 6 we provide the lens galaxy central coordinates as well as the position of the multiple images relative to the lens galaxy location used in the lens modeling. For J100140.12+020040.9 and J095930.93+023427.7, we retrieved the image position from Jackson 2009.

4.2. The mass models

The purpose of the new lens modeling is first, to measure the total mass of the galaxy within R_E: $M(<R_E)$ and second, to check if the environment contribution measured in Sect. 3.2.3 is a good estimator of the external shear.

To do so, we used the Lenstool code (Kneib et al. 1993; Jullo et al. 2007) to model the lens-galaxy mass distributions. Lenstool allows a χ^2 minimization of parametric mass models either in the source or in the image plane. For higher accuracy, we used the image plane minimization algorithm.

4.2.1. SIE+γ

We performed a set of lens model in which the mass distribution that the lens galaxies follows is that of a singular isothermal ellipsoid (SIE). An SIE is defined by its position, velocity dispersion, orientation, and ellipticity. Assuming that mass follows light, we fix the SIE central position to that of the galaxy light profile (Table 6). We chose its orientation to be that of the Sersic bulge light profile (Table 5) with an additional $\pm 10°$ uncertainty to take into account a possible misalignment between the luminous bulge and the DM halo (e.g. Kochaneck 2002). The higher boundary for the SIE ellipticity is set equal to that of the Sersic profile (Table 5); the lowest boundary is set to 0 to take into account a possibly shallower distribution of the DM halo compared to the luminous core observed in ETGs (e.g. Gavazzi et al. 2007).

In addition, we model the contribution of the environment by an "external shear", which is parametrized by the shear strength and orientation. The group and cluster contributions to the shear at the lens galaxy locations are measured in Sect. 3.2.3. We use the values of γ and PA_γ from Table 4, and the corresponding error bars as priors to build the lens models.

Therefore, the total number of free parameters for the models is 5: 3 for the SIE (orientation, ellipticity, velocity dispersion) and 2 for the external shear (strength and direction). The number of observational constraints is 6 for the quads and rings and 4 for the triple image lenses. The χ^2 of the best lens models are reported in Table 7 (Col. 3). The best fit models (with χ^2 in Col. 3) are displayed in Figs. 7 to 11. Whenever $\chi^2 \gg 1$, we have performed a second lens model, changing the priors on the external shear to the following ones: $\gamma = [0.0, 0.9]$, $PA_\gamma = [-90°, 90°]$,

Table 6. Position of the lensing galaxy (in degree) and relative position (in arc-second) of the images used as constraints for the lens mass model.

Lens Image	RA δRA	Dec δDec
COSMOS 0049+5128	150.2052807	1.8578028
A1	*2.05*	*0*
A2	*0*	*2.05*
A3	*0*	*–2.05*
A4	*–2.05*	*0*
COSMOS 5947+4752	149.94955	2.7979502
A1	*2.28*	*0*
A2	*–2.28*	*0*
A3	*0*	*2.28*
A4	*0*	*–2.28*
COSMOS 0038+4133	150.1595	2.6927351
A1	*–0.43*	*–0.33*
A2	*0.00*	*–0.62*
A3	*0.04*	*–0.61*
A4	*0.22*	*0.71*
COSMOS 0124+5121	150.3522	1.8558994
A1	*0*	*0.89*
A2	*0*	*–0.89*
A3	*0.89*	*0*
A4	*–0.89*	*0*
COSMOS 0047+5023	150.19858	1.8397919
A1	*–1.42*	*–1.15*
A2	*0.10*	*–1.56*
A3	*2.08*	*–0.36*
A4	*–0.05*	*0.90*
COSMOS 5941+3628	149.92209	2.6080412
A1	*0.*	*1.24*
A2	*0.*	*–1.24*
A3	*–1.24*	*0*
A4	*1.24*	*0*
COSMOS 0050+4901	150.21104	2.8171935
A1	*1.15*	*0.69*
A2	*–1.53*	*1.10*
A3	*–1.53*	*–0.80*
A4	*0.27*	*1.88*
COSMOS 0018+3845	150.07666	2.6458333
A1	*–0.39*	*–1.15*
A2	*–1.22*	*–0.33*
A3	*1.36*	*0.25*
COSMOS 5914+1219	149.81142	2.2054236
A1	*–0.93*	*–0.45*
A2	*1.26*	*1.43*
A3	*1.81*	*0.55*

hence letting the external shear parameters free. The χ^2 of these second lens models are reported in Table 7 (Col. 4) and referred as $\chi^{2\prime}$.

For J095930.93+023427.7, we modeled the group in direction to the lens by a SIS which position is fixed to the position of the group in the X-ray catalog. Hence, the only parameter allowed to vary is the velocity dispersion of the profile. The best-fit model in Table 7 is obtained for a group with velocity dispersion: $\sigma_v^{\rm group} = 408^{+94}_{-29}$ km s^{-1}, if it was at the lens galaxy redshift. From Fig. 11, we see that the fit is not perfect: with additional observational constraints such as the velocity dispersions of individual group members and of the lens galaxy closest neighbor (to the East), one could perform a more detailed model of the lens potential which would most probably improve the fit.

Systems with perfect Einstein rings are mostly satisfactorily modeled by an SIE plus the measured external shear (COSMOS 5947+4752 in Fig. 7, COSMOS 0124+5121 in Fig. 8, COSMOS 5941+3628 in Fig. 9). The reason is that for those lenses, we arbitrarily chose the image positions: they are symmetrically distributed around the lens. In addition, the SIE ellipticity is allowed to be null. Consequently we are artificially correctly fitting the image positions, whatever the external shear values are (as long as the shear strengths are not too large). For those systems, only the Einstein ring and associated mass are reliable measurements in Table 7.

For COSMOS 0049+5128, the fit is poor ($\chi^2 = 35.3$). If we let the external shear free, the best-fit shear parameters are different from those measured in Sect. 3.2.3. If we subtract the shear vector given in Table 4 from the best-fit shear vector in Table 7 (Col. 4), we find the direction pointing toward the galaxy closest to the lens (Galaxy 2 in Fig. 7). Galaxy 2 is at a projected distance ∼13″ to the lens galaxy. If this were at the lens redshift, it would need to have a velocity dispersion $\sigma_v^{\rm Galaxy2} = 174$ km s^{-1} to create the shear necessary to obtain $\chi^{2\prime}$ while fixing the shear parameters to the measured values.

It is the same for the other lenses: if fixed in the lens model, the external shear produced by the groups leads to $\chi^2 \gg 1$. If we set the shear parameters free, the best-fit shear will point in a direction that corresponds to the vectorial summed orientation of the shear produced by the groups and of the shear produced by a secondary (and third in the case of COSMOS 0038+4133) galaxy. In Table 8 we report the projected distance between the lens galaxy and the secondary (third) galaxy as well as the the velocity dispersion of the second (third) galaxy that is needed to obtain $\chi^{2\prime}$ when fixing the external shear parameters to the one produced by the groups. For COSMOS 0050+4901, the velocity dispersion derived for the main lens and for the secondary galaxy are that of a group rather than that of a galaxy: indeed, when we look at the image of the lens (Fig. 10), we see that the field is crowded with galaxies. However, the neighbor density ratio measured in Sect. 3 does not show any evidence for the presence of a structure at the lens redshift. Therefore, if there is actually a group intervening in this system, it should be at a different redshift than that of the main lens galaxy. For the other systems, the velocity dispersion associated with the secondary lens can be associated with a galaxy mass. For COSMOS 0047+5023, we see in Fig. 9 that the field around the lens is crowded with galaxies: an improved version of the present mass model should take them into account, preferentially using a measurement of their redshift and velocity dispersion.

We conclude that our efforts at measuring the external shear were not in vain because, when using it in the lens model, we clearly identify the missing element: the best fit will point at the closest galaxy to the lens or indicate the realistic presence of a galaxy group in the line-of-sight. We come back to this result in Sect. 5.4.

The Einstein radius of the lens galaxy and corresponding mass were calculated for the best models and are displayed in Table 7.

4.2.2. The proportion of DM in the Einstein radius

We integrated the galaxy light profile density up to the Einstein radius and used the stellar mass of the lens galaxy, identifying the effective radius to the half stellar mass radius, to determine the stellar mass within the Einstein radius, $M_\star(<R_{\rm E})$. Doing so, we can compare it to the total mass within the Einstein radius, $M(<R_{\rm E})$, which was obtained during the lens modeling. This gives us a measurement of the lens galaxy projected DM fraction

Table 7. Best-fit parameters for the lens models: SIE + shear.

Name	N	χ^2	($\chi^{2\prime}$, γ, PA$_\gamma$)	$\sigma_v \pm \delta\sigma_v$	R_E	R_E	$M(<R_E)$	$f_{DM}(<R_E)$
				km s^{-1}	$''$	kpc	10^{11} $M_\odot$	
COSMOS 0049+5128	R	35.3	(5.6, 0.023, +83°)	313^{+7}_{-10}	$2.17^{+0.00}_{-0.06}$	$10.2^{+0.0}_{-0.3}$	$7.31^{+0.11}_{-0.60}$	$0.94^{+0.06}_{-0.03}$
COSMOS 5947+4752	R	1.6	_	326^{+11}_{-6}	$2.33^{+0.00}_{-0.00}$	$11.1^{+0.0}_{-0.0}$	$8.61^{+0.59}_{-0.32}$	$0.95^{+0.06}_{-0.03}$
COSMOS 5921+0638	4	11.8	(2.0, 0.025, +20.5)	189^{+0}_{-1}	$0.62^{+0.00}_{-0.00}$	$4.4^{+0.0}_{-0.0}$	$1.10^{+0.01}_{-0.00}$	$0.58^{+0.00}_{-0.0-}$
COSMOS 0038+4133	4	6.3	(0.5, 0.128, –76.3°)	207^{+23}_{-12}	$0.60^{+0.00}_{-0.00}$	$4.3^{+0.0}_{-0.0}$	$1.41^{+0.31}_{-0.21}$	$-0.37^{+0.05}_{-0.07}$
COSMOS 0124+5121	R	0.9	_	267^{+38}_{-19}	$0.91^{+0.00}_{-0.01}$	$6.8^{+0.0}_{-0.1}$	$3.55^{+1.0}_{-0.52}$	$0.84^{+0.24}_{-0.12}$
COSMOS 0047+5023	4	1283.1	(10.4, 0.126, –15.10°)	383^{+9}_{-38}	$1.80^{+0.00}_{-0.39}$	$13.5^{+0.0}_{-2.9}$	$14.52^{+0.02}_{-3.63}$	$0.68^{+0.00}_{-0.17}$
J100140.12+020040.9	4	7.3	(2.3, 0.053, +0.16°)	259^{+43}_{-18}	$0.81^{+0.01}_{-0.00}$	$6.1^{+0.1}_{-0.0}$	$3.00^{+1.10}_{-0.41}$	$0.60^{+0.22}_{-0.08}$
COSMOS 5941+3628	R	0.5	_	315^{+51}_{-20}	$1.23^{+0.02}_{-0.00}$	$9.3^{+0.1}_{-0.0}$	$6.80^{+2.37}_{-0.80}$	$0.62^{+0.24}_{-0.07}$
J095930.93+023427.7	4	6.8	_	255^{+37}_{-17}	$0.79^{+0.00}_{-0.02}$	$6.0^{+0.0}_{-0.2}$	$2.89^{+0.77}_{-0.38}$	$0.71^{+0.30}_{-0.12}$
COSMOS 0050+4901	4	545.4	(26.3, 0.097, +79.9°)	386^{+82}_{-30}	$1.65^{+0.02}_{-0.00}$	$12.7^{+0.2}_{-0.0}$	$11.88^{+8.99}_{-0.06}$	$0.92^{+0.55}_{-0.18}$
COSMOS 0018+3845	3	45.3	(0.2, 0.103, +39.9°)	289^{+2}_{-0}	$1.32^{+0.01}_{-0.00}$	$10.2^{+0.1}_{-0.0}$	$6.22^{+0.15}_{-0.00}$	$0.93^{+0.00}_{-0.01}$
COSMOS 5914+1219	3	215.9	(0.1, 0.086, +71.2°)	358^{+23}_{-14}	$1.60^{+0.00}_{-0.01}$	$12.8^{+0.0}_{-0.1}$	$12.00^{+1.51}_{-0.87}$	$0.79^{+0.13}_{-0.04}$

Notes. (1) Lens name. (2) Number of images or "R" if it is a complete Einstein ring. (3) χ^2 of the best lens modeled obtained when using the priors on the external shear measured in Sect. 3.2.3. (4) Favorite shear parameters (when the one measured in Sect. 3.2.3 lead to $\chi^2 \gg 1$) and corresponding χ^2. (5) Velocity dispersion of the SIE corresponding to the best model in (4) or in (3) if no other. (6) Corresponding Einstein radius in arc-second and (7) in kpc. (8) Mass of the lens galaxy in the Einstein radius. (9) Fraction of DM in the Einstein radius. In Cols. (5)–(8), the errors are owing to the source redshift uncertainty (as explained in Sect. 3.2.3).

Table 8. Parameters for Galaxy 2.

Name	Distance	$\sigma_v^{\rm Galaxy2}$	Fig.
	$''$	km s^{-1}	
COSMOS 0049+5128	12.8	174	7
COSMOS 0921+0638	1.6	70	8
COSMOS 0038+4133	3.5	195	8
$''$	4.6	195	8
COSMOS 0047+5023	3.9	264	9
J100140.12+020040.9	1.1	94	9
J095930.93+023427.7	4.9	275	11
COSMOS 0050+4901	7.4	366	10
COSMOS 0018+3845	3.5	113	10
COSMOS 5914+1219	3.0	209	10

Notes. (1) Lens Name. (2) Distance between the lens galaxy and Galaxy 2 (or Galaxy 3 in the case of COSMOS 0038+4133). (3) Velocity dispersion of Galaxy 2 (or Galaxy 3) as explained in Sect. 4.2.1. (4) Figure number where the lens model is displayed and Galaxy 2 and 3 are labeled.

within the Einstein radius: $f_{DM}(<R_E) = 1 - \frac{M_\star(<R_E)}{M(<R_E)}$. These values are reported in Table 7. The errors come from the propagation of the uncertainties in $M_\star$, R_e, $M(<R_E)$ and R_E.

The negative DM fraction for COSMOS 0038+4133 may indicate that the stellar mass of the lens galaxy is overestimated. This is surprising, because for this system the photometric and spectroscopic redshifts agree, which therefore made us confident that the SED, and consequently the stellar mass, is reliable as well. Another possible explanation is that the light profile fit is not correct and that we measured too large an effective radius. This is indeed a possible explanation, because a bright ring surrounds the lens galaxy and may bias the determination of the light profile. Finally, it is also possible that the source redshift is lower than the one considered here ($z_s^{\rm min} = 1.5$). Indeed, if $z_s = 0.9$, the total mass in the Einstein radius would be $M(<R_E) = 4.88 \times 10^{11}$ $M_\odot$, and the corresponding DM fraction $f_{DM}(<R_E) = 0.6$. Because of all these questions, which require further investigation, we did not keep this system for the rest of the analysis.

For the 11 remaining systems, the fraction of DM varies between 0.58 ± 0.00 (COSMOS 5921+0638) and $0.95^{+0.06}_{-0.03}$ (COSMOS 5947+4752).

In Fig. 6 we report the evolution of $f_{DM}(<R_E)$ with the redshift. The evolution of $f_{DM}(<R_E)$ with redshift is compatible with constant or slight decreasing. The interpretation of this tendency is linked to the evolution of the Einstein radius, R_E versus effective radius, R_e. Indeed, for a given galaxy if (1) $R_E \sim R_e$, the fraction of dark matter in the Einstein radius is expected to be "low" because, in this case, we are probing the region where the galaxy is baryon-dominated: $f_{DM}(<R_E)$ is then a lower limit of the total f_{DM}. On the contrary, if (2) $R_E \gg R_e$: we are measuring a $f_{DM}(<R_E)$, which is getting close to the total f_{DM}, and therefore it is expected to be larger, on average, than the one determined for (1). This is indeed the case (see Fig. 6, top right panel): $f_{DM}(<R_E)$ increases slowly when R_E/R_e increases. From the same Fig. 6 (bottom left panel) we see that the ratio R_E/R_e increases quickly with redshift, meaning that as the redshift grows we are measuring $f_{DM}(<R_E)$ getting closer to the total f_{DM} of the galaxy. The fact that $f_{DM}(<R_E)$ is slightly decreasing or "at best" constant when the redshift grows, suggests that the "total" fraction of dark matter is genuinely lower in the high-redshift lens galaxies than in the low-redshift lens galaxies.

Interestingly, we observe the same tendency if we consider the lens sample from Jiang and Kochanek (2007, JK07 hereafter): they measure the DM fraction (with or without adiabatic compression in their galaxy models and Salpeter initial mass function (IMF)) in the Einstein radius of 22 galaxies spanning a lens redshift $z_l = [0.0808, 1.004]$. If we look at the 18 galaxies with $R_E/R_e < 10$ as in our sample (see Fig. 6), we notice that similarly to our sample that first, $f_{DM}(<R_E)$ decreases slightly with redshift with the same slope than for our sample (−0.18),

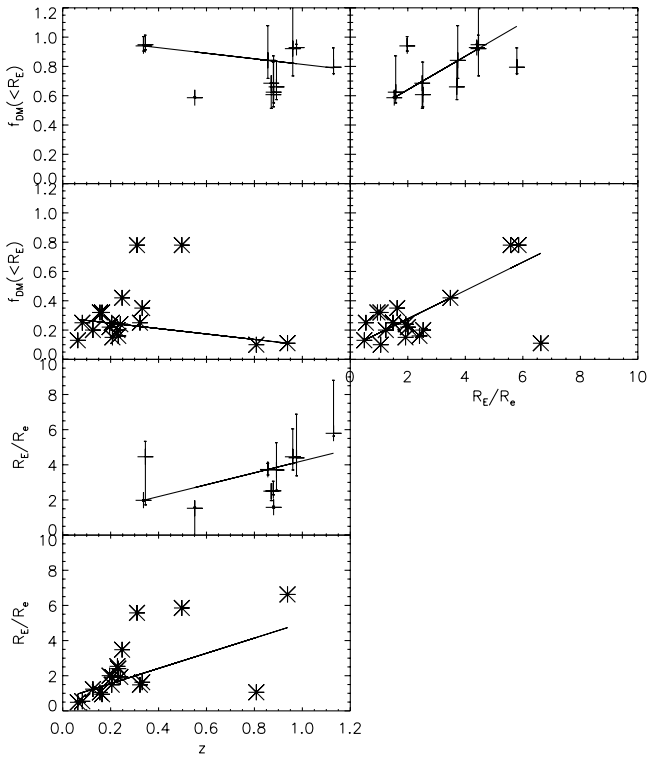

Fig. 6. Evolution of the dark matter fraction and related parameters for two lens samples: COSMOS (crosses) and JK07 (stars). *Top left panels*: evolution of the DM fraction in the Einstein radius with the redshift. The least-deviation fits are displayed (solid lines), and follow the relations $f_{\rm DM}(<R_{\rm E}) = -0.18\times z+1.00$ for COSMOS and $f_{\rm DM}(<R_{\rm E}) = -0.18\times z+0.38$ for JK07. *Top right panels*: variation of the DM fraction as function of the ratio of the Einstein radius versus effective radius. The least-deviation fits give the following relations: $f_{\rm DM}(<R_{\rm E}) = +0.11\times\frac{R_{\rm E}}{R_{\rm e}}+0.41$ (COSMOS) and $f_{\rm DM}(<R_{\rm E}) = +0.09\times\frac{R_{\rm E}}{R_{\rm e}}+0.08$ (JK07). Bottom panels: evolution with redshift of the Einstein radius versus effective radius. The least-deviation fits give the following relations: $\frac{R_{\rm E}}{R_{\rm e}} = +3.4\times z+0.8$ (COSMOS) and $\frac{R_{\rm E}}{R_{\rm e}} = +4.3\times z+0.7$ (JK07). For JK07, we report the results obtained for galaxy models without adiabatic compression. The slopes are similar for models with adiabatic compression.

and second, the radius $R_{\rm E}/R_{\rm e}$ increases with redshift while third $f_{\rm DM}(<R_{\rm E})$ slightly increases when $R_{\rm E}/R_{\rm e}$ increases. The second effect is also observed for eleven ETGs from Strong Lenses in the Legacy Survey (Ruff et al. 2011).

We add that even if the COSMOS sample and the JK07 sample show similar behavior, we chose not to mix them for the display and slope calculations to avoid misinterpretations owing to possible systematics that may affect the measurement of the DM fraction in the two different methods (e.g. different IMFs).

5. Discussion and conclusions

From the analysis of the COSMOS strong-lenses in the redshift range 0.34 to 1.13, we obtain three major results: (1) the lens galaxy stellar masses increase with the redshift, (2) the lens galaxy environments are compatible with those of ETGs in this redshift range and (3) the DM fraction of the lens galaxies in the Einstein radius slightly decreases with the redshift when the ratio between the Einstein radius versus the effective radius strongly increases with redshift. Let us discuss each one of these trends.

5.1. Increase of the lens stellar mass with redshift

In Sect. 2.3 we measured that the lens galaxy stellar mass increases with redshift. Is this a result of the selection method used to built the lens sample? At $z\sim0.4$, one of our lenses has an effective radius of $\sim0.3''$ and at $z\sim0.9$, the smallest lens galaxy effective radius is $\sim0.2''$ (see Table 5). The effective radius is a lower limit for the Einstein radius. These "lower limit Einstein radii" correspond to lower limits in mass within the Einstein radius that are in our case $10^{10.9}$ $M_\odot$ at $z=0.4$ and $10^{11.0}$ $M_\odot$ at $z=0.9$, assuming a source at $z=1.5$. Hence, for a given source redshift, the minimal lens galaxy mass should increase with the lens redshift to be visually detected; consequently, most probably, the minimal stellar mass might increase as well with redshift. Following this reasoning, we expect the sample average stellar mass to increase with the redshift. While this reasoning is simplistic because the source redshifts are different for every lens, it still partially explains the increasing stellar mass with increasing redshift of the lens galaxies. So far, it is not clear whether this "detection bias" effect is the only reason for the lens galaxy stellar mass increase with redshift. This result should be investigated in dedicated numerical simulations (e.g. van de Ven et al. 2009; Mandelbaum et al. 2009).

5.2. Evolution of the lens galaxy environment

Our study of the environments of COSMOS lens galaxies via the projected galaxy number density in Sect. 3.1 indicates that the environment of lens galaxies is similar to that of ETGs across the whole range of redshifts tested here. This result extends the previous measurements made in the redshift range [0.068; 0.513] with the SLACS sample (T09 and Auger 2008). It is particularly interesting because the COSMOS and SLACS samples have very different selection criteria: therefore, this result is most probably a genuine characteristic of strong-lens galaxies rather than a selection bias.

We also notice that both neighbor density estimators tested here appear to be reliable estimators of the environment of galaxies, because X-ray groups and clusters are actually detected around lenses with high $\frac{\Sigma_{10}}{\langle\Sigma_{10}\rangle_r}$ and high $\frac{D_1}{\langle D_1\rangle_r}$ ratios.

5.3. The decreasing dark matter fraction with redshift

We measured the lens galaxy DM fraction in the Einstein radius by combining the total mass in the Einstein radius, the light density profile, and the stellar mass in the galaxy. The projected DM fraction decreases with redshift even though the ratio between the Einstein radius and the effective radius increase with the redshift (see Fig. 6). A similar trend is seen in the lens galaxy dataset of JK07, which covers a similar redshift range. Using toy models and a λCDM cosmology and the SLACS lenses, Napolitano et al. (2010) and Tortora et al. (2010) first noticed that for a fixed stellar mass and age, the DM fraction is similar for high- and low- redshift galaxies. They also noticed that the slope of the distribution of $f_{\rm DM}$ versus age is steeper than explained by their model and invoked different scenarios to interpret the discrepancy (including adiabatic compression and different IMF for different galaxy ages). Another possible effect that could be responsible for the DM fraction decrease with redshift is the increasing stellar density of ETGs with redshift as discussed by Bezanson et al. (2009). But to understand if the results are affected by one of these effects, $f_{\rm DM}$ needs to be measured in comparable radius, not different for each galaxy, contrary to the Einstein radius. Results obtained within the effective radius by

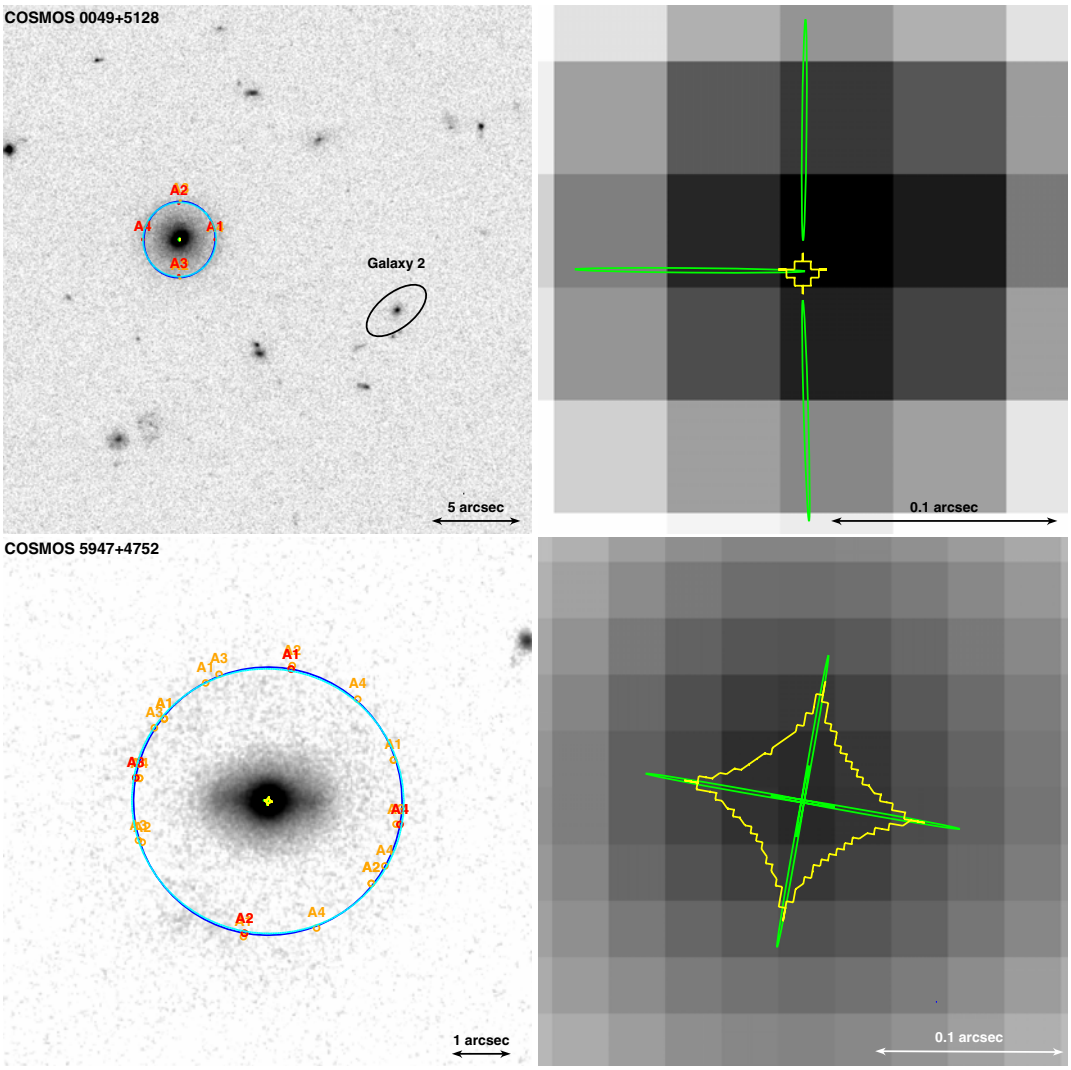

Fig. 7. Mass models overlaid on ACS images for (*top to bottom*) COSMOS 0049+5128 and COSMOS 5947+4752. The *left column* displays the best mass model corresponding to the χ^2 given in Table 7 (Col. 4 or 3 if no other). The *right panel* shows a zoom of the central region of the lens models, where the source can be seen. North is to the top and East to the left. Color code: the red circles are the observed images, whose radii correspond to the position uncertainty used in the modeling. In orange are the images produced by the best-lens model (in case of perfect fit, the orange and red crosses are superimposed). The navy blue lines describe the potential. The caustic lines are in yellow, and the critical lines are in cyan. The green ellipses show the position of the source as seen through the best-mass model (one source for each image; when a good fit is reached, the four sources are partially superimposed). We indicate the position of Galaxy 2 (see Sect. 4.2.1 and Table 8).

Ruff et al. (2011) seem to agree with our conclusions. In order to conclude on the favorite ongoing processes on ETGs since $z \sim 1$ as a function of their age and stellar mass, a joint analysis of the different lens galaxy samples which allow these measurements would certainly be a first step toward a better understanding.

5.4. Some remarks on the lens models

Using lens modeling we measured the Einstein radii and related total masses for the lens galaxies. Doing so, we were able to measure their DM fractions within their Einstein radius. In addition, the lens models were used to test the calculation of the external shear produced by the groups around the lens galaxies. We observed that in every lens model, the difference between the best-fit external shear and the shear produced by the groups points toward the closest galaxy to the lens. We calculate that those secondary galaxies need to have realistic velocity dispersions for the lens models to provide good fits.

Moreover, we have measured that a catalog of high-mass groups and clusters modeled by TIS is giving very similar total shear strengths and orientations than a combination of high-mass and low-mass group catalogs. Therefore we conclude that a measurement of the external shear that affects the lens potential at the lens galaxy location could be made if one could combine a measurement of the redshift and velocity dispersion of the lens galaxy closest neighbor(s) with the locations, masses, and radii of the most massive groups and clusters (such as the one provided by the X-ray observations in the COSMOS field) in a $\gtrsim 5'$ radius around the lens galaxy. By fixing the external shear one would break an important source of degeneracy in the lens models.

5.5. Conclusions

On one hand, we have measured that the environment of lens galaxies is similar to that of non-ETGs over a wide redshift range: between 0.068 and 1.13 if we combine the results from

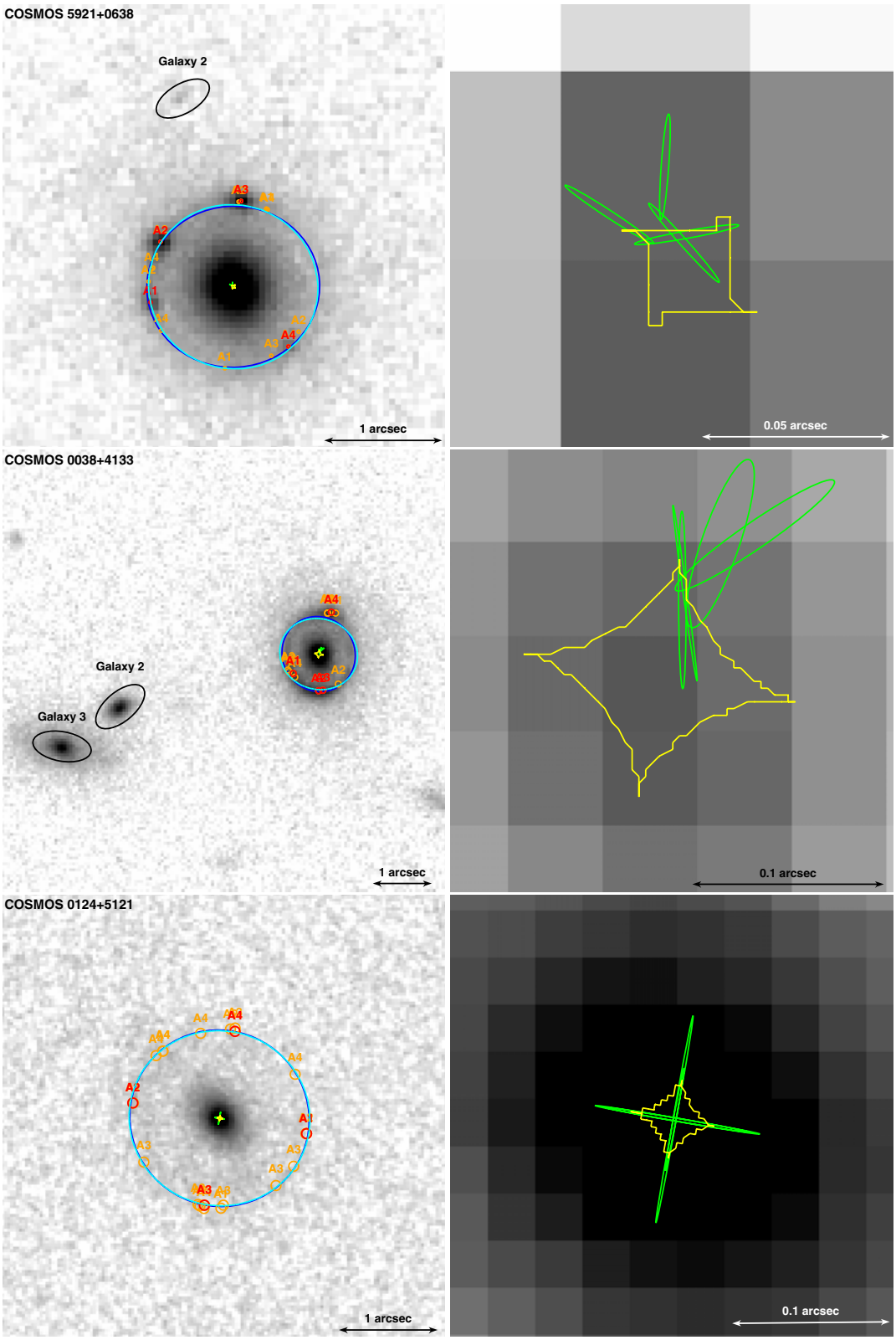

Fig. 8. Suite: mass models on top of ACS images for (*top to bottom*) COSMOS 5921+0638, COSMOS 0038+4133 and COSMOS 0124+5121. The color code for the labels is given in Fig. 7. North is to the top and East to the left.

the SLACS sample (T09, Auger 2008) and from the COSMOS sample (this paper). On the other hand, we have built up an ensemble of clues suggesting that the mass properties of lens galaxies evolve with redshift.

Indeed, at high redshift, lens galaxies have a large stellar mass and a total dark matter fraction $\langle f_{\rm DM}\rangle \sim 0.7$ (for $z > 0.8$). On the contrary, at low redshifts, lens galaxies have lower stellar mass and their DM fraction is $\langle f_{\rm DM}\rangle > 0.8$.

These results argue in favor of high stellar density of the high-redshift ETGs compared to low-redshift ETGs as suggested by the results of Bezanson et al. (2009). Or it could be that the difference between low- and high- redshift lens galaxy

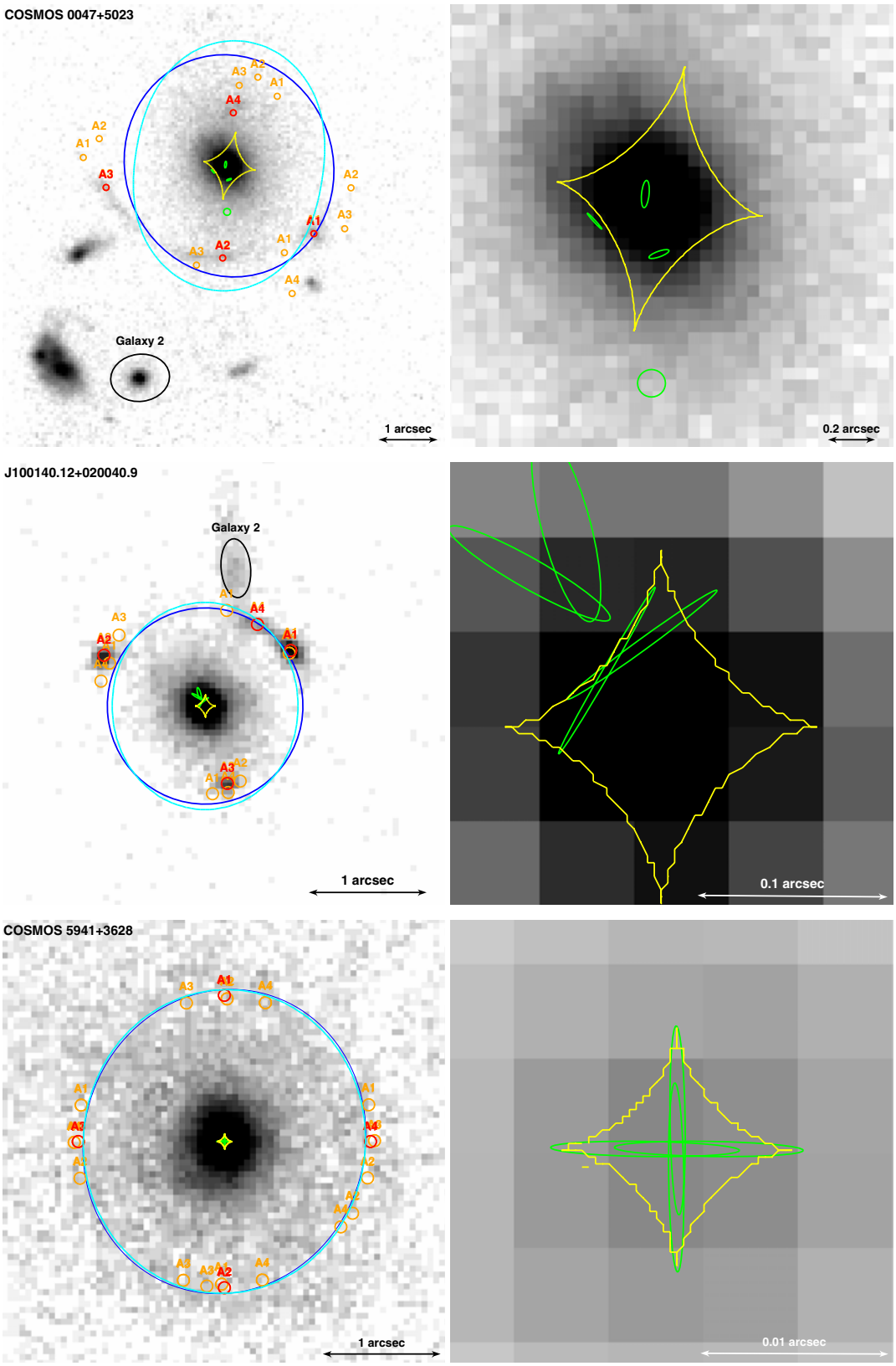

Fig. 9. Suite: mass models on top of ACS images for (*top to bottom*) COSMOS 0047+5023, J100140.12+023427.7 and COSMOS 5941+3628. The color code for the labels is given in Fig. 7. North is to the top and East to the left.

population is a consequence of the stellar population aging and different IMFs at different ages (see Napolitano et al. 2010). It could also be that the effects measured here are related to the lensing efficiency, which in this case would be a complex combination of (1) the lens population number density, (2) the source population distribution in space, redshift, and luminosity, (3) the survey properties (sensitivity, band, size, angular resolution), (4) biases in the lens sample selection.

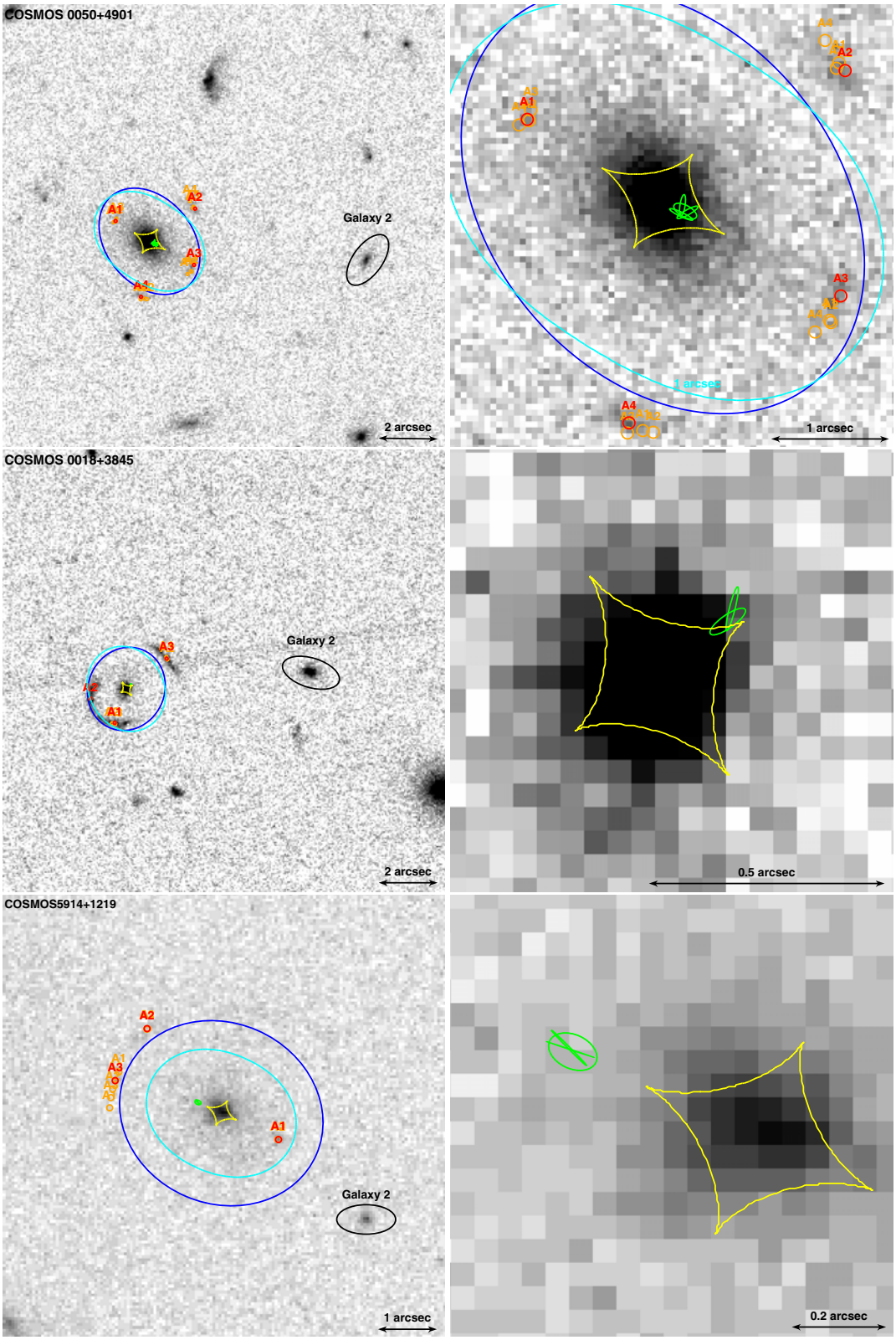

Fig. 10. Suite: mass models on top of ACS images for (*top to bottom*) COSMOS 0050+490, COSMOS 0018+3845 and COSMOS 5914+1219. The color code for the labels is given in Fig. 7. North is to the top and East to the left.

To distinguish between an evolutionary or a pure lensing origin of the effects discovered in this study, the evolution of lens galaxy properties with redshift needs to be studied in dedicated numerical simulations (e.g. van de Ven et al. 2009; Mandelbaum et al. 2009). Whether the effects are intrinsic to the massive early-type galaxy population or to the lensing efficiency, they must be fully understood if one aims to properly study the galaxy properties gathered from lens galaxy populations.

Acknowledgements. We acknowledge the anonymous referee for providing a detailed and very useful report. We are gratefully indebted to M. Limousin and R. Gavazzi for enlightening discussions. D.A. thanks CNRS and CEA for support

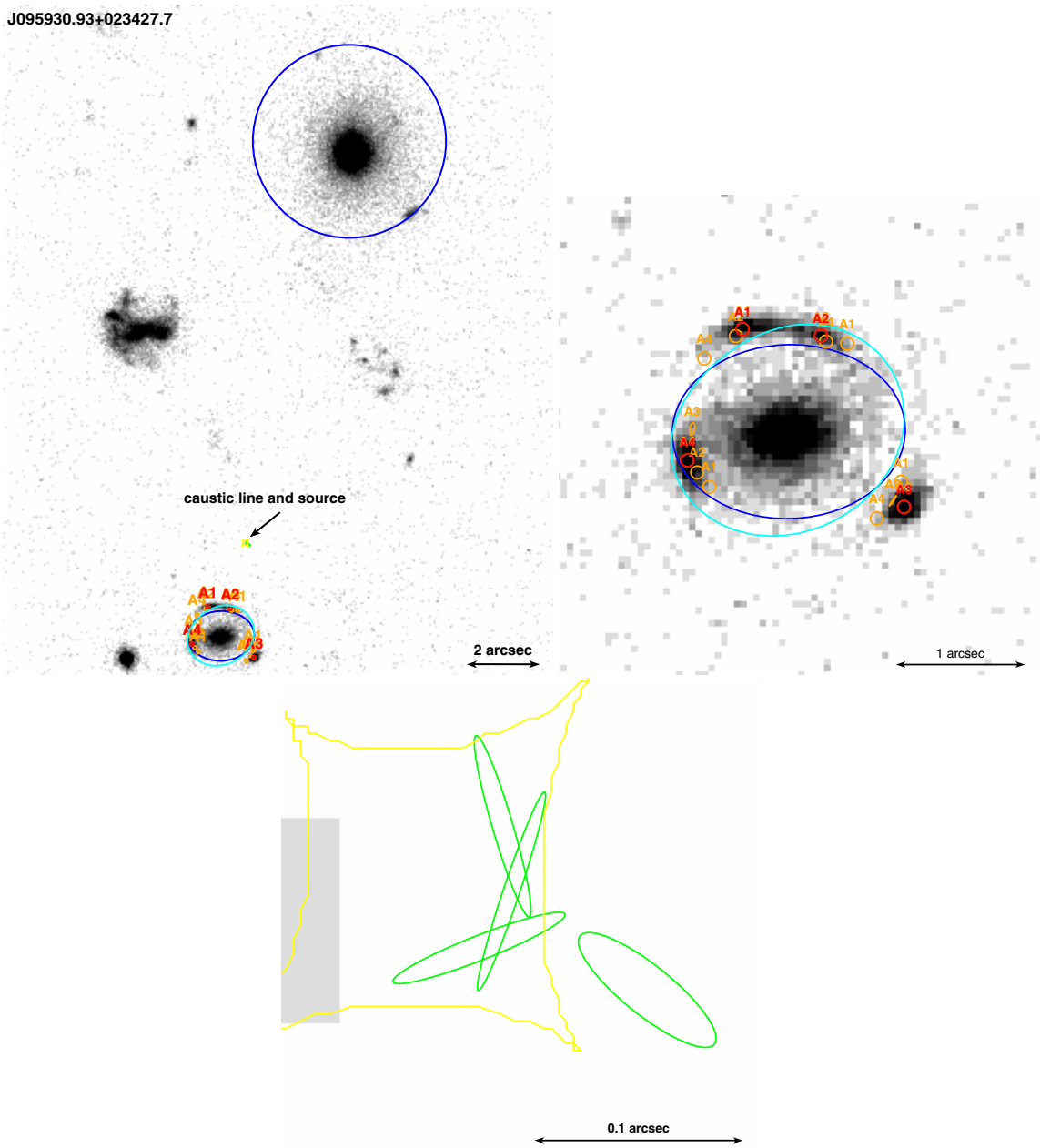

Fig. 11. Suite: mass models for the J095930.93+023427.7. *Top left panel*: the navy blue circle located north of the image surrounds the group central galaxy. *Top right panel*: zoom on the lens galaxy and on the images. *Bottom panel*: zoom on the caustic (yellow curves) and on the favorite source position (green ellipses). The color code for the labels is given in Fig. 7. North is to the top and East to the left.

and visits to the Geneva observatory, where this work was finalized. J.P.K. thanks for support from CNRS and SL2S ANR-06-BLAN-0067 and DESIR ANR-07-BLAN-0228. E.J. acknowledges the support of the NPP, administered by Oak Ridge Associated Universities through a contract with NASA.

References

Allam, S. S., Tucker, D. L., Lin, H., et al. 2007, ApJ, 662, L51
Anguita, T., Faure, C., Kneib, J.-P., et al. 2009, A&A, 507, 35
Auger, M. W. 2008, MNRAS, 383, L40
Bartelmann, M., Meneghetti, M., Perrotta, F., Baccigalupi, C., & Moscardini, L. 2003, A&A, 409, 449
Bezanson, R., van Dokkum, P. G., Tal, T., et al. 2009, ApJ, 697, 1290
Bolton, A. S., Burles, S., Koopmans, L. V. E., Treu, T., & Moustakas, L. A. 2006, ApJ, 638, 703
Bolton, A. S., Burles, S., Koopmans, L. V. E., et al. 2008, ApJ, 682, 964
Bruzual, G., & Charlot, S. 2003, MNRAS, 344, 1000
Bundy, K., Ellis, R. S., Conselice, C. J., et al. 2006, ApJ, 651, 120
Cabanac, R. A., Alard, C., Dantel-Fort, M., et al. 2007, A&A, 461, 813
Capak, P., Aussel, H., Ajiki, M., et al. 2007a, ApJS, 172, 99
Capak, P., Abraham, R. G., Ellis, R. S., et al. 2007b, ApJS, 172, 284
Capak, P., Mobasher, B., Scoville, N. Z., et al. 2011, ApJ, 730, 68
Chae, K.-H., Mao, S., & Kang, X. 2006, MNRAS, 373, 1369
Chantry, V., & Magain, P. 2007, A&A, 470, 467
Dobke, B. M., King, L. J., & Fellhauer, M. 2007, MNRAS, 377, 1503
Elvis, M., Civano, F., Vignali, C., et al. 2009, ApJS, 184, 158
Faure, C., Kneib, J.-P., Covone, G., et al. 2008, ApJS, 176, 19
Faure, C., Kneib, J.-P., Hilbert, S., et al. 2009, ApJ, 695, 1233
Finoguenov, A., Guzzo, L., Hasinger, G., et al. 2007, ApJS, 172, 182
Finoguenov, A., Connelly, J. L., Parker, L. C., et al. 2009, ApJ, 704, 564
Gavazzi, R., Treu, T., Rhodes, J. D., et al. 2007, ApJ, 667, 176
Grillo, C., Gobat, R., Lombardi, M., & Rosati, P. 2009, A&A, 501, 461
Hasinger, G., Cappelluti, N., Brunner, H., et al. 2007, ApJS, 172, 29
Hilbert, S., White, S. D. M., Hartlap, J., & Schneider, P. 2007, MNRAS, 382, 121
Hilbert, S., White, S. D. M., Hartlap, J., & Schneider, P. 2008, MNRAS, 386, 1845

Ilbert, O., Capak, P., Salvato, M., et al. 2009, ApJ, 690, 1236
Ilbert, O., Salvato, M., Le Floc'h, E., et al. 2010, ApJ, 709, 644
Jackson, N. 2008, MNRAS, 389, 1311
Jiang, G., & Kochanek, C. S. 2007, ApJ, 671, 1568
Jullo, E., Kneib, J.-P., Limousin, M., et al. 2007, New J. Phys., 9, 447
Keeton, C. R. 2001, ApJ, 561, 46
Keeton, C. R. 2003, ApJ, 584, 664
Kneib, J. P., Mellier, Y., Fort, B., & Mathez, G. 1993, A&A, 273, 367
Knobel, C., Lilly, S. J., Iovino, A., et al. 2009, ApJ, 697, 1842
Kochanek, C. S. 2002, The Shapes of Galaxies and their Dark, 62
Koekemoer, A. M., Aussel, H., Calzetti, D., et al. 2007, ApJS, 172, 196
Koopmans, L. V. E., Treu, T., Bolton, A. S., Burles, S., & Moustakas, L. A. 2006, ApJ, 649, 599
Lagattuta, D. J., Fassnacht, C. D., Auger, M. W., et al. 2010, ApJ, 716, 1579
Leauthaud, A., Finoguenov, A., Kneib, J.-P., et al. 2010, ApJ, 709, 97
Lilly, S. J., Le Fèvre, O., Renzini, A., et al. 2007, ApJS, 172, 70
Lilly, S. J., Le Brun, V., Maier, C., et al. 2009, ApJS, 184, 218
Limousin, M., Kneib, J. P., Bardeau, S., et al. 2007, A&A, 461, 881
Limousin, M., Sommer-Larsen, J., Natarajan, P., & Milvang-Jensen, B. 2009a, ApJ, 696, 1771
Limousin, M., Cabanac, R., Gavazzi, R., et al. 2009b, A&A, 502, 445
Mandelbaum, R., van de Ven, G., & Keeton, C. R. 2009, MNRAS, 1066
Marleau, F. R., & Simard, L. 1998, ApJ, 507, 585
McCracken, H. J., Peacock, J. A., Guzzo, L., et al. 2007, ApJS, 172, 314
Mobasher, B., Capak, P., Scoville, N. Z., et al. 2007, ApJS, 172, 117
Momcheva, I., Williams, K., Keeton, C., & Zabludoff, A. 2006, ApJ, 641, 169
Natarajan, P., Kneib, J.-P., Smail, I., et al. 2009, ApJ, 693, 970
Napolitano, N. R., Romanowsky, A. J., & Tortora, C. 2010, MNRAS, 405, 2351
Ofek, E. O., Rix, H.-W., & Maoz, D. 2003, MNRAS, 343, 639
Oguri, M., Keeton, C. R., & Dalal, N. 2005, MNRAS, 364, 1451
Ruff, A. J., Gavazzi, R., Marshall, P. J., et al. 2011, ApJ, 727, 96
Sanders, D. B., Salvato, M., Aussel, H., et al. 2007, ApJS, 172, 86
Scoville, N., Aussel, H., Brusa, M., et al. 2007, ApJS, 172, 1
Scarlata, N., Carollo, C. M., Lilly, S., et al. 2007a, ApJS, 172, 406
Scarlata, N., Carollo, C. M., Lilly, S. J., et al. 2007b, ApJS, 172, 494
Simard, L. 1998, Astronomical Data Analysis Software and Systems VII, 145, 108
Taniguchi, Y., Scoville, N., Murayama, T., et al. 2007, ApJS, 172, 9
Tortora, C., Napolitano, N. R., Romanowsky, A. J., & Jetzer, P. 2010, ApJ, 721, L1
Treu, T., Koopmans, L. V., Bolton, A. S., Burles, S., & Moustakas, L. A. 2006, ApJ, 640, 662
Treu, T., Gavazzi, R., Gorecki, A., et al. 2009, ApJ, 690, 670
Vikhlinin, A., Burenin, R. A., Ebeling, H., et al. 2009, ApJ, 692, 1033
van de Ven, G., Mandelbaum, R., & Keeton, C. R. 2009, MNRAS, 1067
Wambsganss, J., Bode, P., & Ostriker, J. P. 2005, ApJ, 635, L1
Wong, K. C., Keeton, C. R., Williams, K. A., Momcheva, I. G., & Zabludoff, A. I. 2011, ApJ, 726, 84